The formation of Ganymede's grooved terrain: Numerical modeling of extensional necking instabilities

Michael T. Bland *, Adam P. Showman

Department of Planetary Science, Lunar and Planetary Laboratory, University of Arizona, Tucson, AZ 85721, USA

Abstract

Ganymede's grooved terrain likely formed during an epoch of global expansion, when unstable extension of the lithosphere resulted in the development of periodic necking instabilities. Linear, infinitesimal-strain models of extensional necking support this model of groove formation, finding that the fastest growing modes of an instability have wavelengths and growth rates consistent with Ganymede's grooves. However, several questions remain unanswered, including how nonlinearities affect instability growth at large strains, and what role instabilities play in tectonically resurfacing preexisting terrain. To address these questions we numerically model the extension of an icy lithosphere to examine the growth of periodic necking instabilities over a broad range of strain rates and temperature gradients. We explored thermal gradients up to 45 K km^{-1} and found that, at infinitesimal strain, maximum growth rates occur at high temperature gradients (45 K km^{-1}) and moderate strain rates (10^{-13} s^{-1}). Dominant wavelengths range from 1.8 to 16.4 km (post extension). Our infinitesimal growth rates are qualitatively consistent with, but an order of magnitude lower than, previous linearized calculations. When strain exceeds ~10% growth rates decrease, limiting the total amount of amplification that can result from unstable extension. This fall-off in growth occurs at lower groove amplitudes for high-temperature-gradient, thin-lithosphere simulations than for low-temperature-gradient, thick-lithosphere simulations. At large strains, this shifts the ideal conditions for producing large amplitude grooves from high temperature gradients to more moderate temperature gradients (15 K km^{-1}). We find that the formation of periodic necking instabilities can modify preexisting terrain, replacing semi-random topography up to 100 m in amplitude with periodic ridges and troughs, assisting the tectonic resurfacing process. Despite this success, the small topographic amplification produced by our model presents a formidable challenge to the necking instability mechanism for groove formation. Success of the necking instability mechanism may require rheological weakening or strain localization by faulting, effects not included in our analysis.
© 2007 Elsevier Inc. All rights reserved.

Keywords: Ganymede; Tectonics; Satellites, surfaces; Jupiter, satellites; Ices

1. Introduction

Covering nearly two-thirds of the satellite, Ganymede's grooved terrain is one of the most tectonically deformed surfaces in the Solar System. First clearly resolved in Voyager images, the grooved terrain consists of series of roughly parallel, periodically spaced ridges and troughs (Fig. 1A) (Smith et al., 1979a, 1979b). Photoclinometric profiles indicate that typical groove sets have a periodicity of 3 to 10 km and amplitudes of 300 to 400 m (Squyres, 1981). Rather than having steep scarps typical of fractures or faults, grooves are undulatory in nature with root-mean-square slopes near 6° and maximum slopes no larger than 20° (Squyres, 1981). Grooves tend to appear in large polygonal swaths 100s to 1000s of km long and 10 to 100 km wide. While grooves generally have consistent spacing and orientation within an individual groove swath, large regions of grooved terrain contain many such swaths, each crosscutting the others at a different orientation.

Digital terrain models of Uruk Sulcus confirm Voyager observations, indicating wavelengths of 2–6 km and amplitudes up to 500 m within the grooved terrain (Giese et al., 1998). However, high-resolution images from the Galileo spacecraft reveal that the grooved terrain is intensely tectonized at scales below the Voyager resolution limit (Fig. 1B) (Pappalardo et al., 1998). Fourier analysis of topography in the Uruk Sulcus region indi-

* Corresponding author. Fax: +1 520 621 4933.
  E-mail address: mbland@lpl.arizona.edu (M.T. Bland).

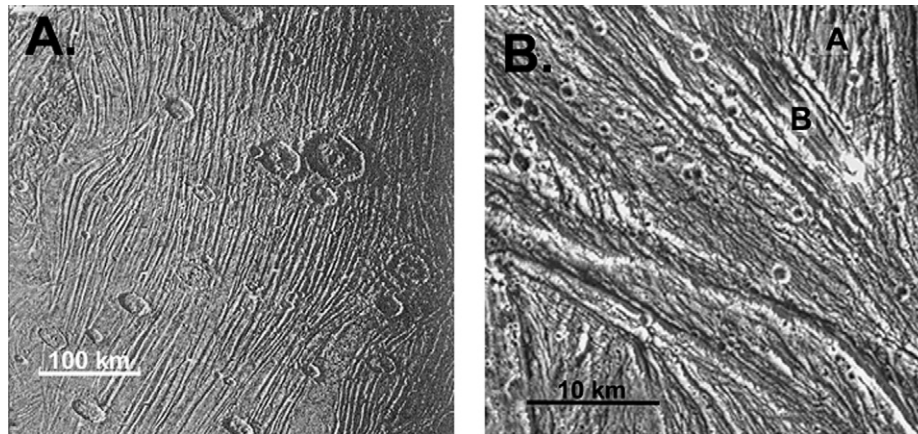Fig. 1. (A) Voyager image of grooved terrain near the south pole of Ganymede. Grooves have a periodic spacing of ~10 km. Illumination is from the right. After Squyres (1982). (B) High resolution Galileo image of grooves in the Uruk Sulcus region (PIA00276, Courtesy NASA/JPL-Caltech). Both Voyager-scale (~10 km wavelength) grooves and finer Galileo-scale (~1 km wavelength) grooves are visible. At high resolution individual groove swaths (labeled 'A' and 'B') are seen to cross-cut and partially disrupt one another implying that groove formation can tectonically resurface preexisting terrain. Note that this high resolution deformation is at a finer scale than the deformation modeled here. Illumination is from the south (bottom). After Pappalardo et al. (2004).

cates that short wavelength (~1 km) deformation is superimposed upon the regional-scale grooves seen in Voyager images (Patel et al., 1999). This small-scale deformation is lower in amplitude than the long-wavelength, Voyager-scale grooves, with heights of ~200 m (Pappalardo et al., 1998).

Based on the lack of identifiable contractional features on Ganymede's surface, most authors accept that the grooved terrain formed by extensional processes during an epoch of global expansion (Squyres, 1982; Golombek, 1982; Pappalardo et al., 1998). The exact cause and magnitude of this expansion remains undetermined. Assuming the grooved terrain to be old, Squyres (1980) suggested that expansion resulted from internal phase changes during differentiation of the satellite. Such volume expansion would increase Ganymede's surface area by 6–7% (Squyres, 1980). A reanalysis of cratering fluxes in the jovian system, however, supports the idea that the grooved terrain formed within the last 2 Ga (Zahnle et al., 2003). While there is much uncertainty in this age constraint, it suggests that expansion could have occurred during a period of tidal heating, after differentiation had ceased, as the Galilean system evolved through a series of Laplace-like resonances (Showman and Malhotra, 1997). The combination of phase transitions and thermal expansion caused by tidal heating would increase Ganymede's surface area by up to 1–2% globally (Showman et al., 1997). Alternatively, if Ganymede entered resonance in a partially differentiated state (like modern Callisto), tidal heating may have induced complete differentiation. The combination of tidal heating and differentiation can produce larger global strains than either mechanism alone. Observations of typical strains involved in the formation of specific groove types indicate that the global change in Ganymede's circumference was large: at least 1.4% but possibly as high as 5.9%, implying increases in surface area of 2.8% to 12.1% (Collins, 2006). These observations support the tidally induced-differentiation mechanism for Ganymede's global expansion.

Despite relatively small values of global strain, significant extensional strain has occurred locally on Ganymede. Reconstruction of presumed tilt-block faulting in Ganymede's Uruk Sulcus region indicates that local strains exceeded 50% at the time of groove formation (Collins et al., 1998b). Furthermore, analysis of strained craters, mostly in dark terrain, shows that rift zones associated with these craters extended by as much as 180% (Pappalardo and Collins, 2005). The apparent conflicting evidence for relatively small values of global strain, but high values of local strain was addressed by Collins (2006) who found that, while the majority of low-relief groove terrain has experienced only a few percent strain, high-relief grooves typically experienced 25% to 50% strain. While these densely spaced, high-relief grooves tend to be thought of as "typical" grooved terrain, they actually represent only ~2–7% of the length of a typical great circle transect of the surface. In contrast, more subdued, low-relief grooves and swaths of smooth bright terrain make up ~45% of a great circle surface transect (Collins, 2006). Thus, values of localized strain between 25% and 100% in regions of high-relief grooves do not violate global strain estimates of order 10% because the majority of the surface has undergone only 1–3% strain. High strains are therefore likely to have been common in regions of high-density, high-relief grooves.

The exact mechanism by which grooves formed remains uncertain. Early work based on Voyager data proposed that the large-scale grooves were extensional fractures or horst-and-graben that were softened by viscous relaxation and mass wasting (Squyres, 1982; Golombek, 1982; Parmentier et al., 1982). While Galileo images indicate that at least some of the structures in the grooved terrain are consistent with horst-and-graben (Pappalardo et al., 1998), these models never adequately explained the strong periodicity of groove spacing within the bright terrain or the undulatory nature of many grooves. To account for these characteristics, Fink and Fletcher (1981) proposed that Ganymede's grooves resulted from the formation of periodic necking instabilities during unstable extension of the icy lithosphere.
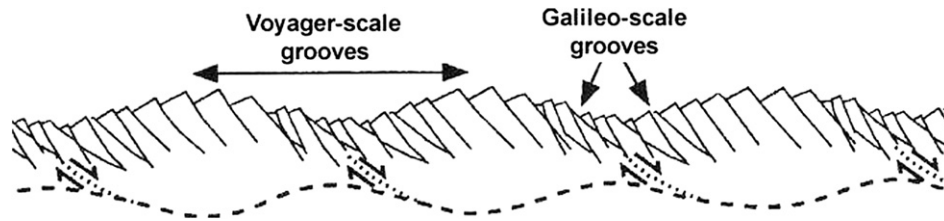
Fig. 2. Cartoon of pinch-and-swell morphology caused by the formation of a periodic necking instability. Small-scale tilt-block normal faulting (Galileo-scale grooves) accommodates the formation of large-scale ridges and troughs (Voyager-scale grooves). Modified from Pappalardo et al. (1998).

The necking instability mechanism models Ganymede's lithosphere as a brittle surface layer underlain by a viscous half-space. When extended, any perturbation in the thickness of the brittle layer may amplify, deforming the lithosphere into a series of periodic pinches and swells (Fig. 2). This mechanism was employed by Fletcher and Hallet (1983) to explain the regular spacing of structures in the Basin and Range province of the western United States. Their semi-analytical, linearized, infinitesimal-strain model utilizes a perturbation analysis wherein a perturbing flow is added to uniform, horizontal extension. The velocity field of each Fourier component of the perturbing flow is calculated separately, allowing the amplitude growth of each component to be independently determined. In general, one Fourier component of the perturbation dominates the flow, growing significantly faster than the other components and producing strongly periodic topography. This dominant wavelength is generally three to four times the thickness of the deforming layer.

Assuming a constant growth rate (defined below) and background strain rate, the amplitude of each Fourier component of the initial perturbation changes exponentially with the form

$$\mathcal{A} = \mathcal{A}_0 \exp\!\big[(q - 1)\dot{\varepsilon}t\big], \qquad (1)$$

where $\mathcal{A}$ is the amplitude of the topography, $\mathcal{A}_0$ is the amplitude of the initial perturbation, q is the exponential growth rate of the Fourier component in question, and $\dot{\varepsilon}t$ is the strain. The growth rate q determines the degree to which instability growth occurs. If $q < 1$, no instability growth occurs and the perturbation decays with time. At $q = 1$, the growth rate of the perturbation exactly matches the rate of lithospheric thinning and topographic amplitudes remain constant. For $q > 1$ the initial perturbation amplifies. Fletcher and Hallet (1983) and Herrick and Stevenson (1990), assuming 10% strain and amplifications ($\mathcal{A}/\mathcal{A}_0$) of 10–100, suggested exponential growth rates (q) of ~40 are needed to produce instability growth consistent with large scale tectonic structures. Allowing for larger values of strain, Collins et al. (1998b) found that growth rates as low as 8–13 are capable of producing ridges and troughs 250–500 m in amplitude.

Herrick and Stevenson (1990) applied the Fletcher and Hallet (1983) model to Ganymede and found that the satellite's high surface gravity and warm temperatures prevented instability growth large enough ($q > 40$) to allow the formation of grooved terrain. This model was later reexamined by Dombard and McKinnon (2001) who incorporated the grain-boundary-sliding (GBS) flow mechanism for ice and lower surface temperatures due to a dimmer young sun and a higher surface

albedo at the time of groove formation and found that, in cases where thermal gradients exceeded 35 K km^{-1} (corresponding to a heat flow of ~80 mW m^{-2}), exponential growth rates and dominant wavelengths of instabilities *are* consistent with ($q > 40$) grooved terrain.

Despite the success of Dombard and McKinnon (2001), the linear stability model suffers from several limitations. The analysis assumes infinitesimal strain and thus treats only the initiation of an instability. Thus, predicting the amplitude of grooves that result from instability growth requires an extrapolation from infinitesimal to finite strain. We expect, however, that nonlinear effects become important as strains become large. If, for example, instability growth creates lateral variations in the thickness of the lithosphere comparable to the lithospheric thickness itself, order unity lateral variations in the deviatoric tensile stress will exist. This causes the system to behave nonlinearly. Numerical models of finite-amplitude compressional folding support the prediction of nonlinear behavior at large strains. These models indicate that growth rates decrease at strains larger than ~10%, in some cases approaching $q = 1$, suggesting a saturation limit to the amount of fold amplification that can occur under finite strain (Zuber and Parmentier, 1996). Furthermore, because the linear stability analysis treats the growth of each Fourier component of the perturbation separately, the Fourier components cannot interact with one another, an effect that may become important at large strains. Because of these limitations, the applicability of necking instabilities to groove formation remains unresolved.

Nonliner modeling of extensional necking instabilities can inform the debate about the mechanism for bright terrain formation (and the removal of older, pre-existing craters). Cryovolcanic (Parmentier et al., 1982; Allison and Clifford, 1987) and tectonic (Head et al., 1997) resurfacing mechanisms have been proposed, and both probably play important roles. Digital elevation models indicate that smooth, low-lying regions exist on Ganymede, suggesting infilling by a low-viscosity cryovolcanic material (Schenk et al., 2001). Liquid water can be pumped to the surface from depths of up to 10 km by topographically induced, subsurface pressure gradients (Showman et al., 2004). This self-limiting pumping mechanism fills low-standing regions with cryovolcanic material while explaining the observed lack of large-scale cryovolcanic flows across high standing regions (Showman et al., 2004). However, some regions of Ganymede's terrain have been predominantly resurfaced by tectonic, rather than cryovolcanic, processes (Head et al., 1997). Observations of truncated groove sets within the grooved terrain support this hypothesis. In these regions, young groove

sets cross-cut and partially or completely destroyed structures in stratigraphically older groove sets (Fig. 1B) (Head et al., 1997). Furthermore, tectonically disrupted craters indicate that resurfacing should occur in cases where strains exceed 15% (Pappalardo and Collins, 2005). Despite these observations, it is not obvious that extensional tectonics can completely destroy preexisting structures. Elucidating how extensional instabilities respond to finite surface topography and large strains is therefore essential to understanding how Ganymede's grooved terrain was formed.

2. The finite-element model

Using the two-dimensional, finite-element model Tekton (version 2.3) in plane strain (Melosh and Raefsky, 1980), we simulate the extension of an icy lithosphere to examine the growth of periodic necking instabilities over a range of strain rates and temperature gradients. Our model incorporates the elastic, viscous, and plastic flow properties of ice. Tekton solves the equations governing the equilibrium between internal stresses and external (applied) forces. These forces are related to the nodal displacement of each element by the Young's modulus E and Poisson ratio ν. We model the elastic properties of ice using a Young's modulus of 10^{10} Pa and a Poisson ratio of 0.25. These values are appropriate for clean, unfractured water ice at terrestrial surface temperatures (Gammon et al., 1983). The sensitivity of our results to variations in the Young's modulus are described in Section 4. The density of ice is assumed to be 980 kg m^{-3}.

In addition to elastic deformation, the model incorporates viscous flow. Although the standard version of Tekton (2.3) does not include a composite flow law, we extended the model to utilize recent laboratory data for the power-law flow of ice to express the total viscous strain rate as (Goldsby and Kohlstedt, 2001; Durham et al., 1997; Kirby et al., 1987)

$$\dot{\varepsilon}_{\text{visco}} = \dot{\varepsilon}_{\text{A}} + \dot{\varepsilon}_{\text{B}} + \dot{\varepsilon}_{\text{C}} + \dot{\varepsilon}_{\text{diff}} + \{1/\dot{\varepsilon}_{\text{GBS}} + 1/\dot{\varepsilon}_{\text{BS}}\}^{-1}, \qquad (2)$$

where subscripts A, B, C, diff, GBS, and BS refer to dislocation creep A, B, and C; diffusion creep; grain boundary sliding; and basal slip. Each of these mechanisms has a temperature and stress dependence of the form

$$\dot{\varepsilon} = \Lambda(1/d)^m \acute{\sigma}^n \exp\{-Q/RT\}, \qquad (3)$$

where $\dot{\varepsilon}$ and $\acute{\sigma}$ are the effective strain rate and deviatoric stress respectively, Λ is a mechanism-dependent constant, d is the

grain size, m is the grain size exponent, n is the power-law exponent, Q is the activation energy, R is the gas constant, and T is the absolute temperature. Diffusion creep is modeled following the approach of Barr and Pappalardo (2005) who cast volume diffusion in the form of Eq. (3) by defining an effective Λ based on the diffusion parameters of Goldsby and Kohlstedt (2001). Table 1 shows the relevant rheological parameters for each rheology. Because Tekton uses a different definition of equivalence than typical creep experiments, the constants Λ_{ex} given in Table 1 should be modified for use in Eq. (3) by multiplying by a factor such that $\Lambda = (3^{(n+1)/2}/2)\Lambda_{\text{ex}}$ (Ranalli, 1995, p. 77). This factor was not included in these simulations; it effect is small, generally less than that introduced by uncertainties in the creep activation energies. Simulations including this correction factor show negligible differences from those without.

Under our simulation conditions, dislocation creep B and C and grain boundary sliding (GBS) dominate the viscous flow. GBS flow is rate limited by the basal slip (BS) flow mechanism such that the slower of the two mechanisms controls the flow [Eq. (2)]. In our simulations, GBS is the slower mechanism, so the presence of the BS flow regime has no impact on model results. Furthermore, Newtonian diffusion, which dominates viscous flow only in warm, low-stress regions, and dislocation creep regime A, which dominates viscous flow only in warm, high-stress regions, minimally affect the model results.

If grain-size-sensitive creep (such as GBS) dominates the viscous flow, the rheology depends heavily on the grain size of the ice. Linear models suggest that, under some conditions, the choice of grain size alone can determine whether instability growth is strong enough to be consistent with groove formation (Dombard and McKinnon, 2001). Unfortunately, we have only poor constraints on the grain sizes present in Ganymede's lithosphere; reasonable possibilities range from 100 μm to 10 cm. Furthermore, grain size most likely is not constant with depth, as high temperatures can increase grain sizes, and high stresses can decrease them. For consistency with published linear models we have chosen a constant grain size of 1 mm for our simulations. We discuss the sensitivity of our results to the choice of grain size in Section 4.

Plasticity is a continuum approach to modeling the brittle behavior of the lithosphere. Plastic rheologies assume that the surface is well fractured at a scale much smaller than the model resolution, and that the deformation resulting from the combined behavior of these fractures can be represented as an ad-

Table 1
Rheological parameters

Creep regime	log Λ_{ex} (MPa^{-n} m^m s^{-1})	m	n	Q (kJ mole^{-1})	Reference
Dislocation creep					
Regime A	11.8	0	4.0	91	Kirby et al. (1987)
Regime B	5.1	0	4.0	61	Kirby et al. (1987)
Regime C	−3.8	0	6.0	39	Durham et al. (1997)
GBS	−2.4	1.4	1.8	49	Goldsby and Kohlstedt (2001)
BS	7.74	0	2.4	60	Goldsby and Kohlstedt (2001)
Volume diffusion	−3.46	2	1.0	59.4	Goldsby and Kohlstedt (2001), Barr and Pappalardo (2005)

dition to the viscous strain rate. We incorporate plasticity into our model via the use of Drucker–Prager yielding in which the yield condition can be written as

$$\sigma_{\text{yield}} = \xi(C\cos\phi - \sigma_m\sin\phi), \tag{4}$$

where C is the cohesion, ϕ is the angle of internal friction, σ_m is the mean stress (negative in compression), and $\xi = 6/[\sqrt{3}(3 - \sin\phi)]$. If the square root of the second invariant of the deviatoric stress tensor within a given finite-element exceeds σ_{yield}, plastic flow initiates, and an additional term ($\dot{\varepsilon}_{\text{plastic}}$) is added to Eq. (2). The elements in which plastic flow can occur are not determined a priori. Instead, the local stress state completely determines when and where the onset of plastic behavior occurs. This permits plastic flow, and thus higher strain rates, to localize in regions of high stress (i.e., in necked regions).

Using a cohesion (C) of 10 MPa and an angle of internal friction (ϕ) of 30°, the strength profile of the lithosphere is defined as

$$\sigma_{\text{yield}} = 12\text{ MPa} - 0.69\sigma_m, \tag{5}$$

which conforms to "Byerlee's rule" for a simple geologic stack. The strength profile given by Eq. (5) has an intercept value one order of magnitude higher than the laboratory-measured profile of Beeman et al. (1988), which has the form

$$\sigma_{\text{yield}} = 1.2\text{ MPa} - 0.65\sigma_{zz}. \tag{6}$$

The use of a high cohesion value permits significant instability growth over a wide range of free parameters (e.g., temperature gradients, and strain rates) and therefore allows examination of how those parameters effect instability growth. An analysis of the dependence of our results on the choice of cohesion value is included below (Section 4).

We assume a linear temperature gradient within Ganymede's lithosphere. We explore temperature gradients ranging from 5 to 45 K km^{-1}, spanning the range of geologically plausible heat flows on Ganymede during groove formation. Except at the surface, isotherms are initially horizontal. Following Dombard and McKinnon (2001), who argued that a weaker sun and higher surface albedo at the time of groove formation reduced surface temperatures on Ganymede relative to present conditions, we use a surface temperature of 70 K in all of our simulations. These temperatures likely represent the minimum plausible surface temperatures during groove formation (Dombard and McKinnon, 2001). Low surface temperatures are particularly favorable to instability growth (Dombard and McKinnon, 2001). The effect of surface temperature on instability growth rates is described in Section 4. To insure numerical stability, we cut off the linear temperature increase with depth at 180 K; at depths greater than this point, the domain becomes isothermal. The exact value of the cut-off temperature used, within a range of 180–210 K, does not affect model results. Cut-off temperatures above 210 K can cause numerical instabilities to occur. The transition to an isothermal temperature profile is consistent with, but somewhat colder than, the thermal profile expected in a thick convecting ice layer; however, our model does not include convection. Nor does it include conduction, a process

that can be important in some cases. The effects of including conduction are discussed in Section 3.4.

We model the dynamics of extension over three orders of magnitude in background strain rate from 10^{-12} to 10^{-15} s^{-1}. Long computational times prevent the examination of even lower strain rates. We apply 31.5% extension to each simulation. As described above, such strains are consistent with strain measurements in regions of high-density, high-relief grooves. The combination of strain rates and total strains imply total extension timescales of 10^4 to 10^7 yrs. Because domains undergo finite extension at a constant velocity (described below), the background strain rates described above do not remain constant in time for a given simulation but decrease by ∼24% as the domain elongates. For the sake of familiarity, we retain the strain rate terminology in the discussions below with the caveat that all strain rates refer to the initial strain rate imposed on the domain.

We use a timestep of 0.1, 1, and 10 yrs for simulations with times of 10^4, 10^5, and 10^6 yrs or greater, respectively. These timesteps fall below the shortest Maxwell times found in our models (∼300 yrs). Decreasing the timestep produces minimal changes in nodal displacements, only ∼10% of the dimensions of a single element, and thus has no bearing on the overall deformation produced by the model.

Our finite-element domains are generally 40–100 km long, 12–24 km deep, and utilize square elements 333 or 167 m on a side. Our results are weakly dependent on the mesh resolution used: final deformation amplitudes vary by 6–7% when resolution is increased by a factor of 2. However, these small variations do not affect our general conclusions. Domain lengths and resolutions permit a broad range of deformation wavelengths to develop. A small amplitude (usually 10 m), sinusoidal topographic perturbation is imposed on the top surface of the domain to allow the instability to initiate. In general, we use domain lengths that are an integral number of half wavelengths of the initial perturbation. However, the initial perturbation is phase shifted to prevent symmetry planes from aligning with domain edges. This helps reduce numerical edge effects (described below). Domain depths insure that the effects due to the bottom boundary are negligible. Extension results from a horizontal fixed displacement boundary condition on the left side of the domain and a horizontal constant velocity boundary condition on the right. Both the left and right sides of the domain use a vertical free slip condition to allow extensional thinning to occur. The bottom of the domain utilizes a free slip condition in the horizontal direction and a fixed displacement condition in the vertical.

We apply a constant gravitational acceleration of 1.4 m s^{-2} to the model, which we initialize by allowing stress to relax towards a purely hydrostatic state. In the upper 6 km of the domain, however, stresses never fully relax to hydrostatic due to the cold surface temperatures. While σ_{zz} (vertical normal stress) conforms to a hydrostatic relationship, σ_{xx} and σ_{yy} (horizontal normal stress) are less compressive than hydrostatic. Thus the mean stress in this region is up to 40% lower than a purely hydrostatic case would predict. This, in turn, reduces the yield stress by up to 12%. However, upon extension, stresses

in the upper region of the mesh quickly become tensional rather than hydrostatic (see below) suggesting that the effect of this initial deviation from a purely hydrostatic model is small.

3. Results

3.1. Form of the instability

The deformation produced by extension of our model domain is consistent with the formation of a necking instability. Simulations produce a pinch-and-swell morphology in which deformation at the surface is inverted (of opposite sign) from the deformation at depth (Fig. 3). Plastic deformation is focused within the pinched regions, illustrating that increased yielding, and thus higher stress, occurs within the thinned portions of the lithosphere. Despite the focusing of plastic deformation within these regions, no obvious localization of plastic flow occurs along narrow fault-like planes.

Both the dominant wavelength and the total amplitude of the deformation depend heavily on the temperature gradient (Figs. 4A, 4C, and 4D) and strain rate (Figs. 4A and 4B) imposed on the simulation. Dominant instability wavelengths vary from 1.8 (Fig. 4C) to 16.4 km (Fig. 4D) with maximum crest to trough amplitudes of approximately 75 m (Fig. 4A). Small edge effects are present in our simulations. These edge effects take the form of an increase or decrease in groove amplitude of up to 20% at the edges of the domain (Fig. 4). We detect no systematic variation in the degree to which groove amplitudes at the domain edges differed from the "average" groove amplitude in a simulation. Furthermore, the effects were not reduced by shifting the phase of the sinusoidal topography. For this reason, calculations of total amplification reported in this paper disregard the topography at edges of the domains.

Lateral variations of the stress field also match our expectations of a necking instability (Fig. 5A), with stresses deviating strongly from hydrostatic. Elements within the top 5 km of the lithosphere contain both compressional and tensile stresses. Compressive stresses result from gravitationally driven hydrostatic stress, and thus align vertically and increase with depth. Horizontally directed tensile stresses dominate the near surface elements and focus within the pinched regions of the lithosphere, being 7–9% greater in groove troughs than in groove crests (Fig. 5B). This preferential concentration of tensile stress leads to the growth of the necking instability. Greater stress in the pinched regions promotes more frequent plastic deformation (i.e., more strain), which further decreases the thickness of the pinched region, localizing more tensile stress and reinforcing the positive feedback that drives the instability. At depths greater than ∼5 km, hydrostatic stress dominates, and both principal stresses become compressional.

The magnitude of the local strain also varies across the domain (Fig. 6). In the near surface, maximum strains ($\varepsilon_I \sim 0.5$) occur within the topographic troughs and minimum strains ($\varepsilon_I \sim 0.05$) occur within topographic crests. These strains are primarily extensional. This distribution of strain agrees with the conception of lithospheric necking shown in Fig. 2. As in our simulations, high degrees of extension occur in Voyager-scale
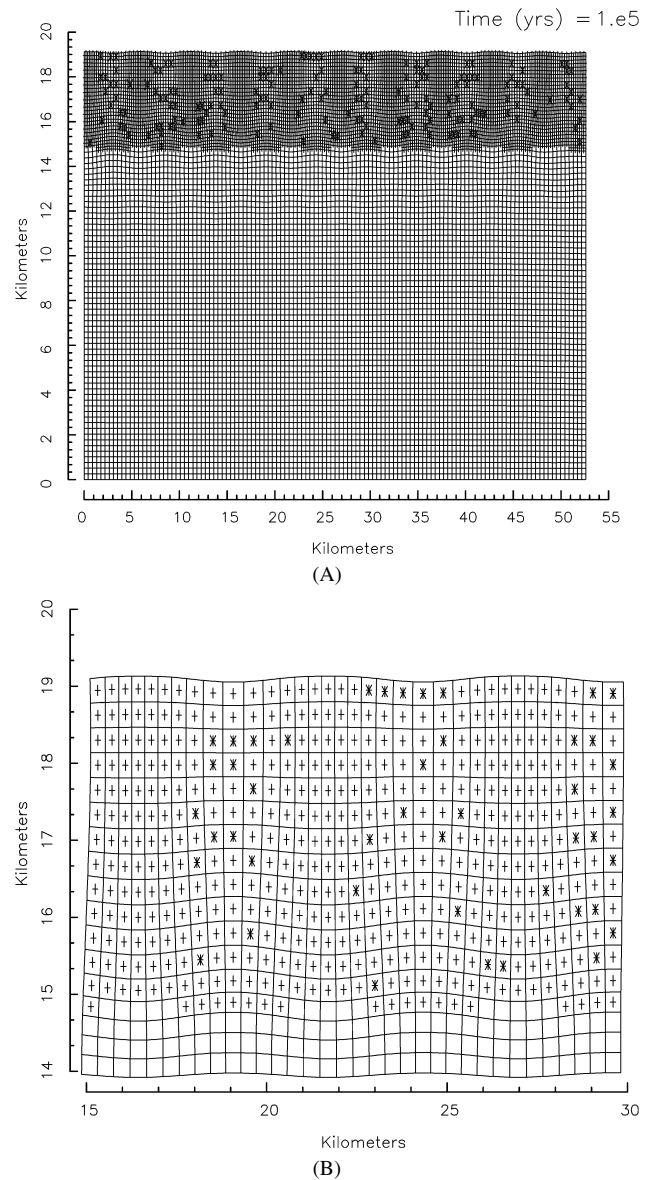

Fig. 3. (A) Deformed finite-element model after 31.5% extension illustrating the degree of deformation at the surface and at depth. The shaded layer indicates where plastic deformation has occurred at any point during the simulation, while black elements indicate where plastic flow has occurred in the most recent timestep. (B) Enlargement of surface deformation showing material contours that were originally horizontal and vertical but are now deformed into pinches and swells. Asterisks indicate elements in which plastic flow has occurred in the most recent time-step. Plus signs indicate where plastic flow has occurred at any point during extension. The scattered distribution of plastic behavior reflects the fact that plastic failure relaxes local stresses back below the yield stress. These stresses require several timesteps (∼3 or 4) to rebound far enough above the yield stress for plastic flow to occur again. Thus while the layer as a whole behaves plastically, only a fraction of the individual elements undergo plastic deformation in a given timestep. Vertical exaggeration is 2:1 in both (A) and (B).

troughs and low degrees of extension occur in Voyager-scale crests (Pappalardo et al., 1998). At depth the strain pattern in our simulations is reversed from that at the surface, with maximum strains occurring beneath topographic crests and minimum strains occurring below topographic troughs. This pattern indicates that the "pinch-and-swell" morphology produced by
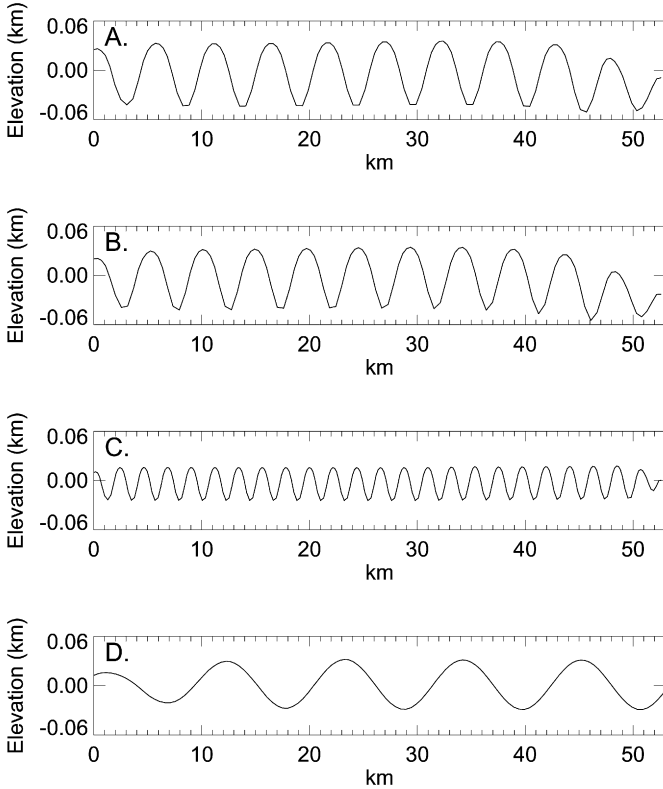
Fig. 4. Typical topographic profiles produced by our simulations for a range of initial conditions: (A) $dT/dz = 15$ K km^{-1} and $\dot\varepsilon = 10^{-13}$ s^{-1}. (B) $dT/dz = 15$ K km^{-1} and $\dot\varepsilon = 10^{-14}$ s^{-1}. (C) $dT/dz = 45$ K km^{-1} and $\dot\varepsilon = 10^{-12}$ s^{-1}. (D) $dT/dz = 5$ K km^{-1} and $\dot\varepsilon = 10^{-15}$ s^{-1}. Each model was initialized with a single sinusoidal perturbation with an amplitude of 10 m. Domains were strained by 31.5%.

our necking instability is not vertically symmetric and may result from flow at depth accommodating necking at the surface.

3.2. Infinitesimal strain

We first examine the effect of infinitesimal strain on instability growth. To do this, we calculate exponential growth rates (q) of our simulated necking instabilities at small strains. We impose an initial perturbation consisting of a single sine wave of known amplitude and wavelength on a domain with a specific thermal gradient and strain rate. As extension occurs, we extract and Fourier transform topographic profiles of the surface to produce power spectra of the deformation. At small strains, the power spectra are strongly unimodal, with a peak at the imposed perturbation wavelength. These spectra provide a measure of the growth of the initial perturbation amplitude as a function of strain and allows calculation of exponential growth rates. The determination of exponential growth rates is only valid in the case where q is a constant, requiring strains to be small. We calculated growth rates after 3% extension, which is sufficient to allow accurate measurement but small enough to avoid the non-linear behavior expected at large strains. Amplitude growth at these strains is in excellent agreement with Eq. (1). This method is consistent with linear models in both the use of small strains and the examination of the growth of each Fourier component of the initial perturbation individually.
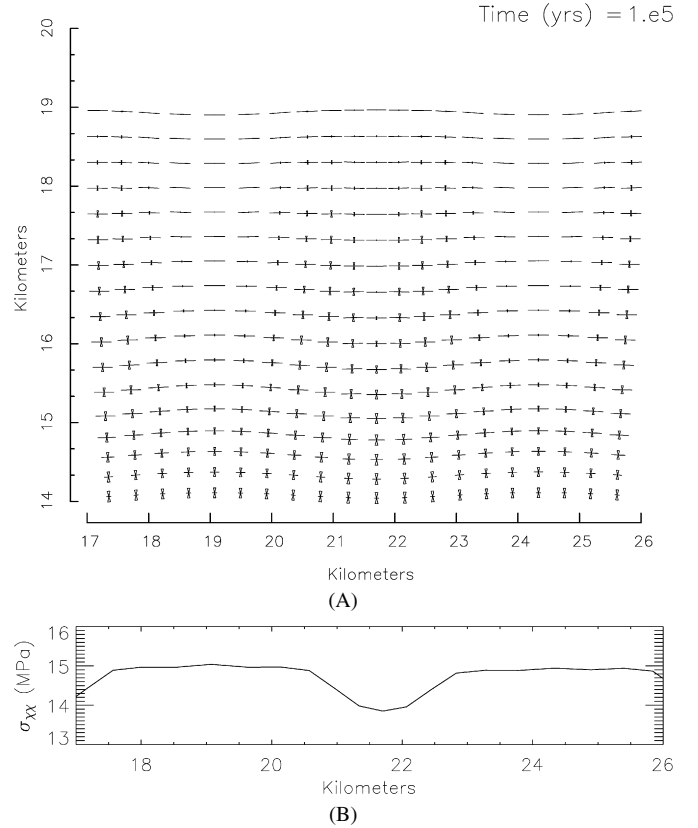

Fig. 5. (A) Orientation and relative magnitudes of principal stresses for a simulation with $dT/dz = 15$ K km^{-1} and $\dot\varepsilon = 10^{-13}$ s^{-1} extended by 31.5% (Fig. 4A). A two-part symbol designates the principal stress in each element, one part for each principal stress. Hour glass shapes indicate compression, while lines indicate extension. The orientation of the symbol aligns with the orientation of the two principal stresses. (B) Profile of horizontal stress (σ_{xx}) across the surface of the domain. The figures show only a small portion of the total domain.

Repetition of this procedure for a range of initial perturbation wavelengths permits measurement of the growth rate as a function of initial perturbation wavelength, $q(\lambda)$, for a particular thermal gradient and strain rate. We can then determine both the wavelength that amplifies the fastest (λ_d) and the maximum growth rate (q) for those particular conditions. Fig. 7 is an example of a $q(\lambda)$ curve, and indicates that for an initial perturbation amplitude of 10 m, temperature gradient of 15 K km^{-1} and strain rate of 10^{-13} s^{-1} the dominant wavelength is 4.44 km and the maximum growth rate is 8.9. While the $q(\lambda)$ curve shown in Fig. 7 is typical of our simulations, the exact width of each curve varies as function of the temperature gradient. Low temperature gradients produce wide, broadly peaked $q(\lambda)$ curves in which a relatively large range of wavelengths have growth rates close to the maximum. High temperature gradients produce narrow, sharply peaked $q(\lambda)$ curves in which deviations from the dominant wavelength as small as 25% produce little or no instability growth. This implies that, if the initial perturbation contains multiple topographic wavelengths, high temperature gradients better amplify a single dominant wavelength than low temperature gradients (see Section 3.6).

The amplitude of the initial perturbation imposed on our simulations influences the magnitude of the growth rates calcu-
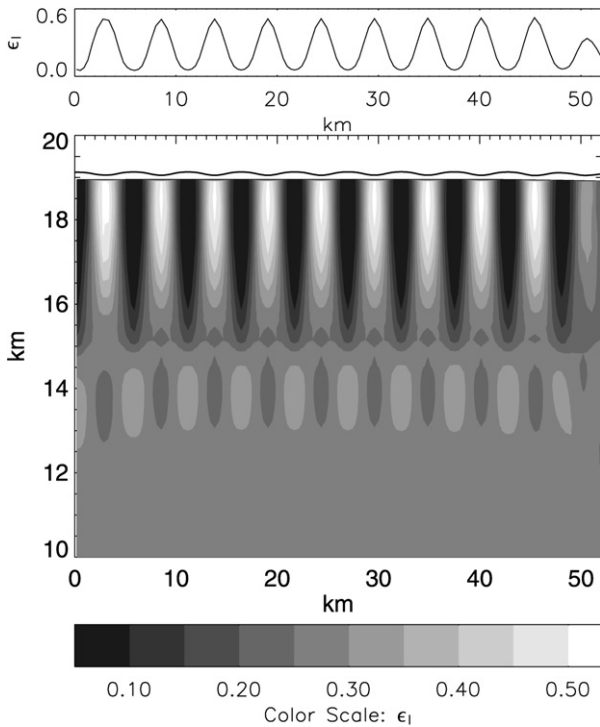
Fig. 6. Grey-scale gives the square root of the second invariant of the total strain ($\varepsilon_I = \sqrt{\frac{1}{2}(\varepsilon_{xx}^2 + \varepsilon_{yy}^2) + \varepsilon_{xy}^2}$) within a domain extended by 31.5%, at a strain rate of 10^{-13} s^{-1} and a temperature gradient of 15 K km^{-1} (Fig. 4A). The surface deformation is plotted as a heavy black line in the gray-scale plot, and only the top half of the domain is shown. The surface trace of ε_I is shown above the gray-scale plot.
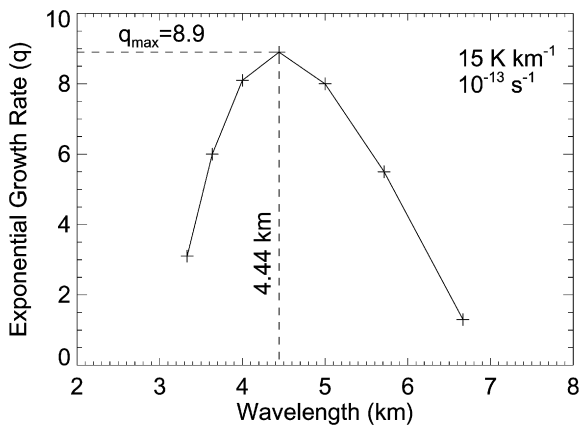

Fig. 7. Exponential growth rate (q) as a function of the wavelength (λ) of the initial 10 m-amplitude perturbation imposed on the domain for a model with a temperature gradient of 15 K km^{-1} and strain rate of 10^{-13} s^{-1}. Dashed lines indicate values of the dominant wavelength (λ_d) and the maximum exponential growth rate (q) for this set of physical parameters.

Fig. 8. (A) Contour plot of dominant wavelength λ_d in kilometers (dashed contours) and exponential growth rate q (solid contours) as a function of temperature gradient and strain rate at infinitesimal strain (3%). (B) Contour plot of total amplification (ratio of the amplitude of the final deformation to the amplitude of the initial perturbation) at finite strain (31.5%). Dominant wavelengths show only modest changes at finite strains. Diamonds indicate parameter values of the simulations.

lated from these infinitesimal strain simulations. Decreasing the perturbation amplitude to 1 m increases growth rates for high temperature gradient simulations, but decreases growth rates for low temperature gradient simulations. At a temperature gradient of 45 K km^{-1}, q increases from 11.5 with a 10 m-amplitude perturbation to 12.7 with a 1 m-amplitude perturbation. In contrast, at a temperature gradient of 5 K km^{-1}, q decreases from 6.6 with a 10 m-amplitude-perturbation to 5.3 with a 1 m-
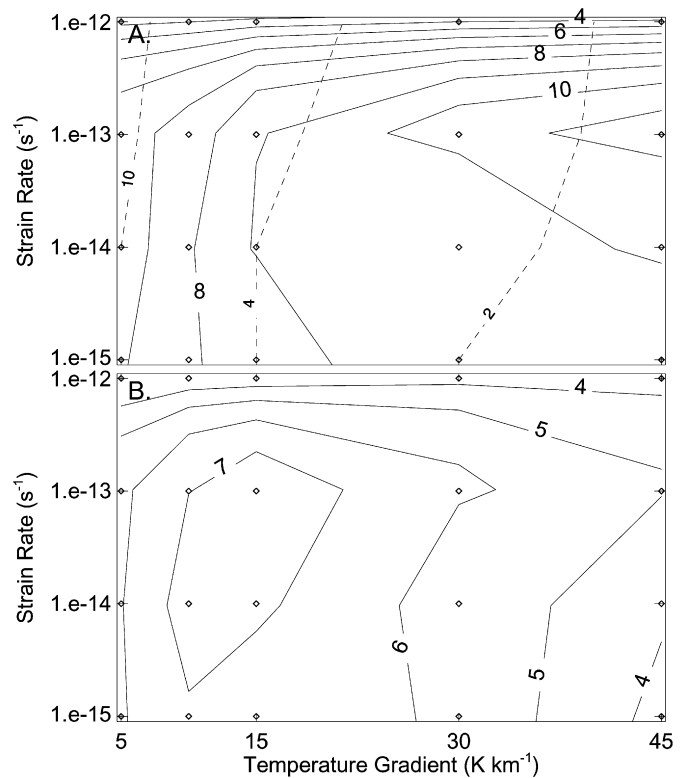
amplitude-perturbation. Why growth rates depend on the amplitude of the initial perturbation remains unclear; however, this dependence suggests that all exponential growth rates calculated from our model have uncertainties of $\sim$1.5.

Using the methods described above, we calculated dominant wavelengths and maximum growth rates for the entire temperature-gradient and strain-rate parameter space, assuming an initial perturbation amplitude of 10 m (Fig. 8A). Dominant wavelengths decrease with increasing temperature gradient and decreasing strain rate, with λ_d ranging from 12.5 km at a temperature gradient of 5 K km^{-1} and strain rate of 10^{-12} s^{-1} to 1.4 km at a temperature gradient of 45 K km^{-1} and strain rate of 10^{-15} s^{-1}. Exponential growth rates, q, increase with increasing temperature gradient and are a maximum at moderate strain rates (10^{-13} s^{-1}). Values range from a maximum of 11.5 at a temperature gradient of 45 K km^{-1} and strain rate of 10^{-13} s^{-1}, to a minimum of 2.3 at a temperature gradient of 5 K km^{-1} and strain rate of 10^{-12} s^{-1}. The increase in exponential growth rates with increasing temperature gradient is qualitatively consistent with previous linearized, infinitesimal-strain models, which also show a preference for moderate to low strain rates (Herrick and Stevenson, 1990; Dombard and McKinnon, 2001).

Despite their qualitative similarities, however, our numerical results differ quantitatively from previous linear model results.

At a given temperature gradient and strain rate, the numerical model produces dominant instability wavelengths a factor of two to three shorter than those calculated from the linear model. If H is the thickness of the layer in which plastic flow has occurred, then $\lambda_d/H \sim 1$–1.5 for the full range of temperature gradients used in our simulations, rather than 3 or 4 as predicted by linear models (Fletcher and Hallet, 1983). Our smaller ratio is most likely caused by the increase in the strength of the lithosphere with depth, which results in an effectively thinner layer. This depth dependence was not included in the linearized models. Our numerical model also produces maximum exponential growth rates, q, an order of magnitude lower than growth rates calculated from linear models, which found that growth rates of 100 or more are possible at high thermal gradients (Dombard and McKinnon, 2001). The difference in magnitude between our numerical results and previous linearized, semi-analytical results is not consistent across the parameter space. The results of the two models are most similar in cases in which both the temperature gradients and strain rates are low (the lower left quarter of Fig. 8A), differing by as little as a factor of two. The difference increases with both increasing temperature gradient and increasing strain rate, with a difference in magnitude of up to a factor of fifteen both at high strain rates (10^{-12} s^{-1}, top of Fig. 8A), and at high temperature gradients and low strain rates (bottom right corner of Fig. 8A).

Our results, therefore, represent a significant departure from the results of previous linear models; however, we feel that this difference results from a more accurate representation of the rheological behavior of ice rather than from shortcomings of the numerical model. We emphasize that the numerical results described in this subsection occur at small strains, so nonlinear effects do not cause the discrepancy with the linear model results. Instead, differences in the implementation of the plastic rheology can probably account for the different model behavior. The linear model invokes plasticity by defining a near-surface layer in which the power-law exponent (n) of the rheology described by Eq. (3) is high ($\sim 10^6$). The relationship between stress (σ) and strain rate ($\dot{\varepsilon}$) in Eq. (3) can be written in the generalized form $\dot{\varepsilon} = \Gamma \sigma^n$. If we assume that the strain rate is related to the stress by a constant that depends on the yield strength with the form $\Gamma = D\sigma_{\text{yield}}^{-n}$, where D is a constant with units of s^{-1}, the relationship between the stress and the strain rate becomes

$$\dot{\varepsilon} = D(\sigma/\sigma_{\text{yield}})^n \tag{7}$$

(Patterson, 1969). This model approximates plastic behavior for large values of n since if $\sigma > \sigma_{\text{yield}}$, the strain rate is nearly infinite, and if $\sigma < \sigma_{\text{yield}}$, the strain rate is negligible. This formulation is a tractable representation of pure plasticity and so is a reasonable choice for analytical models. However, Eq. (7) is not equivalent to true plasticity. The problem lies in the choice of the constant D that relates the stress ratio ($\sigma/\sigma_{\text{yield}}$) to the strain rate. Clearly, if $\sigma = \sigma_{\text{yield}}$, the strain rate depends sensitively on this parameter since, for this value, $\dot{\varepsilon} = D$. However, the physical interpretation of D is unclear. In contrast, Tekton provides a more realistic formulation of plastic behavior in which the magnitude of the plastic strain rate depends on

the local stress field and a stress-relaxation timescale (Owen and Hinton, 1980). This formulation of plastic flow generates lower, but more physically meaningful growth rates than the formulation described above. Furthermore, we again note that the numerical model uses a depth-dependent yield stress while that in Dombard and McKinnon (2001) was depth-independent, and this difference may also cause some differences in the behavior of the two models.

Unlike our numerical model, the linear model also does not include elasticity. Because of this, all of the strain in the linear model partitions into plastic or viscous deformation. In the numerical model, however, strain partitions into elastic as well as viscous and plastic deformation. This reduces exponential growth rates in the numerical model because the plastic strain is the major contributor to necking instability growth in our simulations. The importance of elasticity is illustrated by simulations in which the Young's modulus is two orders of magnitude higher than typical ice values; increasing the Young's modulus decreases the role of elasticity in the model since $\varepsilon_{\text{elastic}} \propto (1/E)$, where $\varepsilon_{\text{elastic}}$ is the elastic strain and E is the Young's modulus. As described in Section 4, increasing the Young's modulus significantly increases the total amplification produced by extension. The inclusion of elasticity's damping effects appears essential to understanding the growth of necking instabilities, thus exponential growth rates calculated from linear models without elasticity may be artificially high.

We emphasize that, while our growth rates are significantly smaller than previous calculations, they are still consistent with the requirement suggested by Collins et al. (1998b) that q must be greater than ~ 8–13 to form Ganymede's grooves. Thus simulations of necking instabilities at infinitesimal strain continue to support the concept that Ganymede's grooves formed via extensional necking. As we describe below, however, nonlinear behavior at finite strains works to curtail the formation of grooves and presents a formidable challenge to groove formation via extensional necking.

3.3. Finite strain

Although large temperature gradients ($dT/dz \geqslant 45$ K km^{-1}) promote high *initial* growth rates, the formation of large amplitude grooves at finite strain actually occurs most easily at intermediate temperature gradients (~ 10–15 K km^{-1}). Fig. 9 shows the amplitude growth of the dominant wavelength of a necking instability for two different temperature gradients at large strains. These curves were constructed using the Fourier analysis method described above, and each plots the growth of the wavenumber that dominates the surface deformation of the extended domain. Here, the 'wavenumber' we use is simply one over the number of wavelengths that fit into a domain (the 'per-domain wavenumber'); note that a constant per-domain wavenumber corresponds to a wavenumber expressed as the inverse of the wavelength in kilometers (the 'per-km wavenumber') that decreases as the domain extends. In both simulations, amplitudes initially increase exponentially [as expected from Eq. (1)], but exponential growth is not sustained outside the infinitesimal strain regime. Instead, growth rates
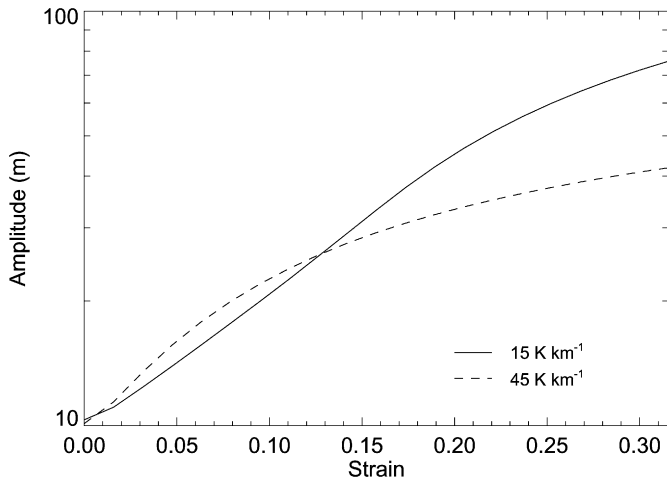
Fig. 9. Amplitude of the per-domain wave number (see text) that dominates the final surface deformation as a function of strain for two models with different thermal gradients (15 and 45 K km^{-1}), each with an initial 10 m-amplitude perturbation consisting of a single sinusoid of the corresponding expected dominant wavelength. In this figure, exponential growth would plot as a straight line. We note that plotting the amplitude of the per-km wave number yields qualitatively identical results. Because the amplitudes derived from the Fourier analysis (shown here) include edge effects (see text) while the amplitudes measured by direct measurement of deformation do not, amplitude values here vary slightly from those described elsewhere.

decrease sharply at finite strain, approaching $q = 1$. These results indicate that nonlinearities play a crucial role in instability growth at strains exceeding ∼10%. Linear extrapolation of initial growth rates, therefore, overpredicts actual groove heights. For example, at a temperature gradient of 45 K km^{-1} and strain rate of 10^{-13} s^{-1} the initial growth rate determined from our infinitesimal strain models is 11.5. Using this initial growth rate to extrapolate to 31.5% strain predicts the formation of 270 m tall grooves. Instead, because growth rates decrease at large strains, these conditions produce grooves only 42 m tall, ∼15% as tall as predicted by infinitesimal-strain models.

The fall-off in exponential growth rate occurs at lower groove amplitudes for higher temperature gradients (Fig. 9). In the 45 K km^{-1} temperature-gradient simulation, the growth rate of the dominant wavelength (1.67 km) begins to decrease after only 7% extension ($\mathcal{A} \sim 13$ m), leading to a maximum amplitude of 42 m after 31.5% extension. For a similar simulation with a temperature gradient of 15 K km^{-1} the growth rate of the dominant wavelength (4.44 km) only begins to decrease after 20% extension ($\mathcal{A} \sim 40$ m), leading to a maximum amplitude of 76 m after 31.5% extension. Thus, in the limit of large strains, the early fall-off in growth rate at high temperature gradients allows low temperature gradient simulations with low initial growth rates to produce more amplification than high temperature gradient simulations with high initial growth rates.

The fall-off in growth at high temperature gradients results in a shift in the ideal conditions for producing large-amplitude grooves to lower temperature gradients than predicted by linear models. Contours of total amplification ($\mathcal{A}/\mathcal{A}_0$) at large strain (31.5%), illustrate this fact (Fig. 8B). An extrapolation of the growth rates calculated at infinitesimal strain (Fig. 8A) predicts that the greatest amount of amplification should oc-

cur at temperature gradients of at least 45 K km^{-1}. However, the actual maximum amplification occurs at 15 K km^{-1} producing 7.6-fold amplification of the initial 10 m perturbation after 31.5% strain. Amplification depends only weakly on the strain rate with a slight preference for moderate strain rates near 10^{-13} s^{-1}.

Because the conditions for maximum amplification depend on a balance between rapid growth at high thermal gradients and sustained growth at low thermal gradients, the exact values of temperature gradient and strain rate at which the maximum amplification occurs depends strongly on the total amount of strain imposed on the model. If strains are small, high thermal gradients are desired such that growth occurs rapidly during the brief period of extension. If large strains are imposed, low thermal gradients that produce sustained growth throughout the extension are preferable. Thus the physical conditions that produce a given groove amplitude are nonunique. One must therefore use caution when attempting to constrain the geophysical conditions that produced specific groove sets on Ganymede.

Two independent mechanisms appear to cause the fall-off in growth at large strains. First, amplitude growth becomes saturated because of the finite thickness of the deforming layer. Mass conservation suggests that the maximum crest to trough amplitude that can be formed by pinching an initially horizontal layer is on the order of the layer thickness itself. In reality, because instability growth can produce more deformation at depth than at the surface (in some cases by more than 50%), the maximum crest to trough amplitude of *surface* deformation will be some fraction of the layer thickness. The thickness of the deforming layer is primarily controlled by the temperature gradient of the lithosphere. Thus, growth fall-off due to amplitude saturation occurs at smaller strains (lower groove amplitudes) in high-thermal-gradient, thin-lithosphere simulations than in low-thermal-gradient, thick-lithosphere simulations.

Second, the increasing wavelength of the deformation as strains become large, and the finite width of the $q(\lambda)$ growth curve combine to limit amplitude growth. As extension begins, a necking instability forms with a particular dominant wavelength (the peak of $q(\lambda)$ curve). As strain continues, the wavelength of the topography will continually increase with the extending domain, moving off the peak of the $q(\lambda)$ curve until, eventually, the surface deformation is substantially longer than the dominant wavelength and instability growth declines. Because the $q(\lambda)$ curve is broad for low temperature gradients and narrow for high temperature gradients (see Section 3.2), the growth fall-off occurs earlier for high temperature gradient simulations than for low temperature gradient simulations. Furthermore, as extension occurs, thinning of the lithosphere increases the thermal gradient causing the dominant wavelength to shift towards shorter wavelengths and away from the extending wavelength of the growing topography. Thus, at finite strains, the wavelength of the surface deformation and the wavelength of dominant growth migrate away from each other.

There is evidence that both of these processes are occurring in our simulations. Amplitude saturation effects are seen when comparing simulations with an initial perturbation amplitude of 1 m to the 10 m perturbation simulations already

described. In the 1 m-amplitude simulations, instability growth occurs exponentially through 17% strain for all temperature gradients. Only at higher strains do the highest temperature gradient (thinnest lithosphere) simulations begin to show a decrease in growth rate. In contrast, in the 10 m-amplitude simulations (Fig. 9), high temperature gradient simulations exhibit a fall-off in growth rate at strains as low as 7%. Thus we find that small initial perturbations can amplify extensively before reaching the saturation limit while large amplitude perturbations quickly saturate. However, even small amplitude initial perturbations show some decrease in growth at large strains. Growth fall-off at these small amplitudes is not likely due to amplitude saturation effects and must therefore be caused by the wavelength of deformation moving off the peak of the $q(\lambda)$ curve.

3.4. Effect of heat conduction

Our model does not include conduction (Section 2), but we *can* estimate how it would affect our results. Employing a simple model in which the timescale for heat conduction, τ, across a layer of thickness H is given by $\tau = H^2/\kappa$, where κ is the thermal diffusivity (Turcotte and Schubert, 2002) we find that $\sim 3 \times 10^6$ years are required to conduct heat across a layer 10 km thick, a thickness consistent with the lithospheric thicknesses of our low temperature gradient simulations. This suggests that, at low temperature gradients, only the lowest strain-rate runs are affected by heat conduction because extension occurs faster than heat can conduct out of the layer. Higher temperature gradient simulations have lithospheric thicknesses closer to 1 km. The timescale for conduction across such a layer is $\sim 3 \times 10^4$ years. Thus at high thermal gradients, heat conducts out of lithosphere faster than extension occurs at all but the vary highest strain rates we examined.

Without conduction, extensional thinning effectively increases the thermal gradient in the lithosphere. The relative increase in thermal gradient is equal to the relative decrease in layer thickness, which is equal to the relative increase in domain length. Thus, in our simulations the temperature gradient increases by 31.5% over the course of extension. With conduction, simulations with high thermal gradients and low strain rates (i.e., when conduction occurs much faster than extension) would maintain their initial thermal gradient because any increases in temperature at a given depth (due to extensional thinning) would quickly decay back to the original thermal profile. Thus, after 31.5% extension, our low strain rate simulations have a higher temperature gradient than they should if conduction were included.

We can use these ideas to infer how conduction would affect our simulations. Amplification contours at high thermal gradients and low strain rates (lower right portion of Fig. 8B) would therefore shift to lower temperature gradients. While our quantitative results (e.g., the thermal gradient at which maximum amplification occurs) may be slightly modified, our qualitative results would likely remain unchanged. Because growth rates in Fig. 8A are calculated after only 3% extension, these values would be unaffected by the inclusion of heat conduction.

3.5. Effect of the initial perturbation

The initial topographic perturbation influences instability growth. If the expected dominant wavelength produced by a particular thermal gradient and strain rate differs significantly from the wavelength of the imposed initial perturbation, complex wavelength interactions can occur. The most interesting type of deformation occurs when the imposed wavelength is somewhat longer (by a factor of $\geqslant 1.4$) than the dominant wavelength. At these values, extension amplifies overtones of the imposed perturbation wavelength (generally half the imposed wavelength) rather than the dominant or imposed wavelengths themselves. Fig. 10 shows a simulation in which we imposed an initial wavelength much longer than the expected dominant wavelength (Fig. 10A). Instead of simply failing to amplify the initial perturbation as expected from the linear model, extension amplifies an overtone wavelength half as long as the imposed perturbation, producing two wavelengths of deformation in the resulting topography (Fig. 10B). Fig. 10C shows the amplitude growth for wavelengths of the imposed perturbation (initially 6.67 km—solid line), half the imposed perturbation (initially 3.33 km—dash–dot line), and the expected dominant wavelength (4.44 km—dashed line) as a function of strain. Both the imposed perturbation and the expected dominant wavelength show minimal growth with increasing strain, but half the imposed perturbation wavelength shows significant amplification
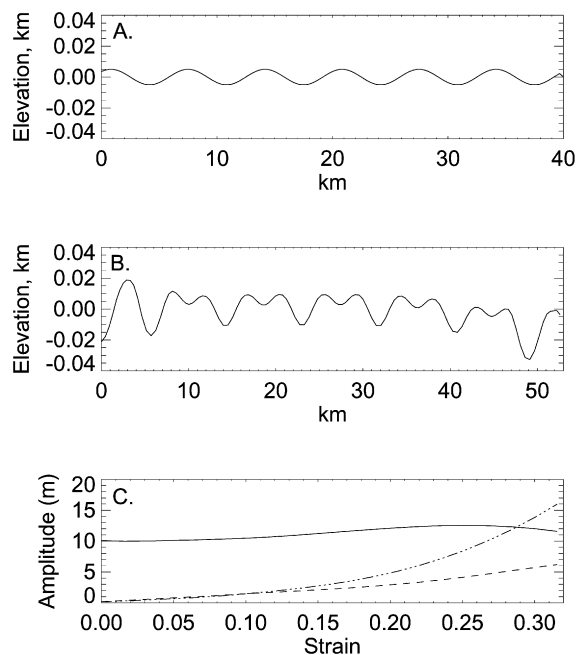

Fig. 10. Illustration of the effect of initial perturbation on instability growth. (A) Topographic profile of the initial perturbation of 6.67 km-wavelength imposed on a domain with physical conditions favoring growth of a 4.44 km-wavelength perturbation. (B) Profile of final surface deformation after 31.5% extension. The final morphology is a superposition of the initial perturbation wavelength and an overtone of half the initial perturbation wavelength. (C) Amplitude growth as a function of strain for the per-domain wavelengths of the initial perturbation (initially 6.67 km—solid line), the dominant wavelength (initially 4.44 km—dashed line), and half the initial perturbation wavelength (initially 3.33 km—dot-dashed line).
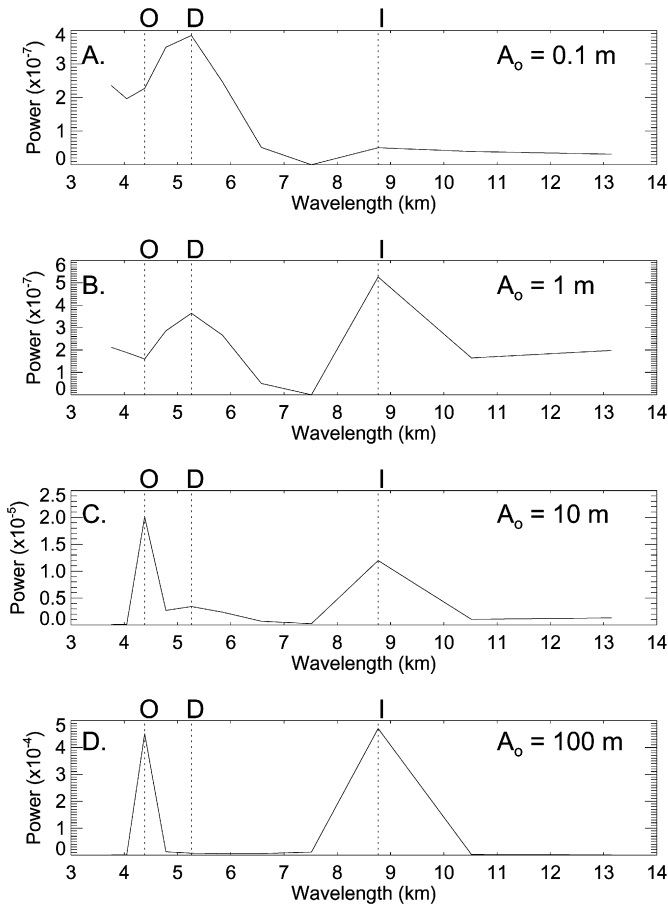
Fig. 11. Illustration of the effect of initial perturbation amplitude ($\mathcal{A}_0$) on wavelength interactions. Power spectra of four simulations with temperature gradients of 15 K km^{-1}, strain rates of 10^{-13} s^{-1}, and total strains of 31.5% are shown in which the wavelength of the imposed perturbation (initially 6.67 km, which becomes 8.77 km after 31.5% extension) is significantly different than the dominant wavelength expected (5.26 km) for the conditions of the model. The simulations differ only in the amplitude of the initial perturbation. Initial perturbation amplitudes are (A) 0.1 m, (B) 1 m, (C) 10 m, and (D) 100 m. The dominant ('D'), imposed ('I'), and overtone ('O') wavelengths are indicated by dotted lines.

at large strain, increasing from an amplitude of ∼0 m to an average amplitude of ∼15 m.

The amplitude of the initial perturbation strongly affects the results described above (Fig. 11). At small initial perturbation amplitudes (Fig. 11A), the imposed perturbation does not influence instability growth and the deformation wavelength equals the dominant wavelength. As the initial perturbation amplitude increases, however, its influence, along with that of its overtone, on the resulting topography increases (Figs. 11B, 11C, and 11D). These results suggest that the imposed perturbation must have an amplitude of at least 10 m before the imposed wavelength, rather than the expected dominant wavelength, controls the wavelength of the deformation.

These results indicate that instability growth on Ganymede depends not only on the conditions present during the most recent groove forming event, but also on the entire extensional history of the region. For example, if a small amount of extension occurs with a low lithospheric thermal gradient, moderate-amplitude, long-wavelength deformation occurs at

the surface. If a later period of extension occurs with a higher thermal gradient, the pre-existence of long wavelength topography on the surface, rather than the physical conditions within the lithosphere, controls the wavelength of the deformation produced by the extension. Observations of Ganymede support such complex groove histories (Collins et al., 1998a). Inferences of the physical conditions that produced a given groove set must therefore carefully consider the entire strain history of the region.

3.6. Nonperiodic initial perturbations

Numerical modeling of extensional necking instabilities allows a detailed investigation of how the presence of multiple wavelengths of topography affects instability growth. As previously noted, linear, infinitesimal-strain models are limited to examining the growth of each Fourier component of the initial perturbation independently. In reality, the pre-grooved surface of Ganymede contained a large number of topographic wavelengths simultaneously. The finite width of the $q(\lambda)$ curve shown in Fig. 7 indicates that, if present, a range of wavelengths, rather than a single dominant wavelength, will amplify as extension occurs. These simultaneously growing wavelengths may interact as topographic amplitudes become large. To investigate this interaction, we performed simulations in which the initial perturbation contained multiple wavelength components. These simulations provide insight into how extensional necking can contribute to the tectonic resurfacing of long-wavelength, preexisting terrain by modifying random initial topography into periodic ridges and troughs.

We created an initial perturbation containing 16 wavelengths ranging from 10 to 1.25 km, which were each given a random phase shift, added together and renormalized to have a maximum peak to trough amplitude of 15 m. Figs. 12A and 12B show the resulting perturbation and a power spectrum of the topography. The Fourier approach to monitoring amplitude growth was again used, allowing the growth of each component of the deformation to be tracked separately.

Figs. 12C and 12E show topographic profiles of the deformation caused by extending such a domain by 31.5%, at a strain rate of 10^{-13} s^{-1}, for temperature gradients of 15 and 30 K km^{-1}, respectively. Power spectra derived from these profiles are shown in Figs. 12D and 12F. Both the topographic profiles and their spectra indicate that growth of the necking instability has removed ($q \leqslant 1$) both the longest and shortest wavelength components of the initial perturbation while strongly amplifying a small range of wavelengths. Changing the temperature gradient within the model lithosphere results in significantly different surface deformation. The 15 K km^{-1} model produces a dominant wavelength of ∼5 km and a maximum crest to trough amplitude of ∼60 m suggesting amplification of the initial perturbation by a factor of 4–6. The 30 K km^{-1} model has a dominant wavelength of ∼3 km and maximum crest to trough amplitudes of ∼45 m. The decrease in the amplitude of the deformation at higher temperature gradients matches our expectations from the finite strain modeling described above (Section 3.3). Since the two models utilized the same initial
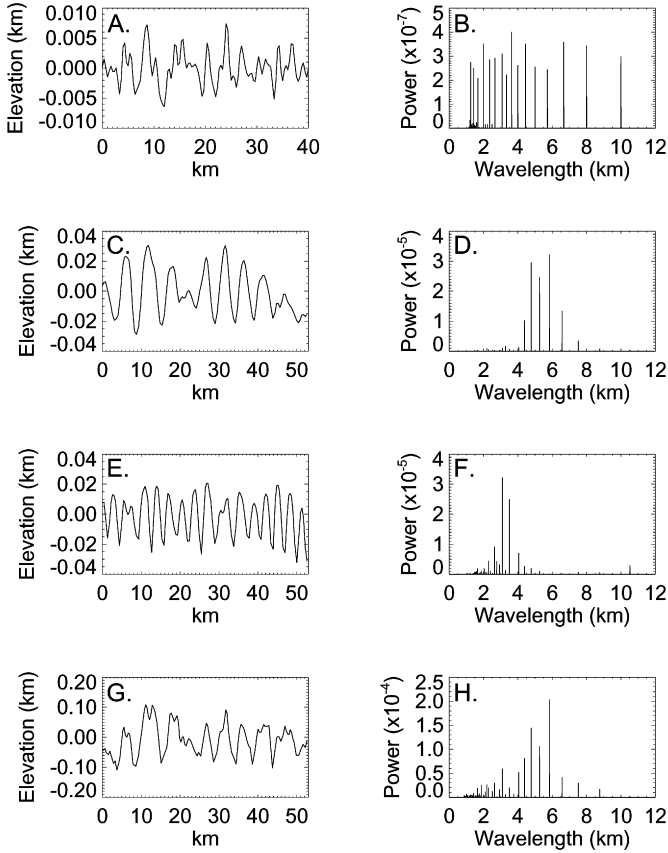
Fig. 12. Demonstration of a necking instability's potential for modifying preexisting terrain. The initial perturbation (A and B) is composed of 16 wavelengths between 1.25 and 10 km. Topographic profiles and power spectra of the final surface deformation after 31.5% extension are shown for a simulation with a temperature gradient of 15 K km^{-1} (C and D) and 30 K km^{-1} (E and F). The effect of initial perturbation amplitude is illustrated by a simulation with a 150 m amplitude perturbation and a temperature gradient of 15 K km^{-1} (G and H). In all cases the strain rate was 10^{-13} s^{-1}.

perturbation, the differences in their final deformation results from differences in the physical conditions of the lithosphere. Furthermore, changing the phase shifts of the included wavelengths of topography has a negligible effect on the final form of the deformation. Thus, it is clear that only the wavelengths present in the topography, rather than its specific shape plays a significant role in instability growth.

Careful examination of the growth of the "removed" wavelengths indicates that they have exponential growth rates $\leqslant 1$. Therefore, rather than the dominant wavelength simply outgrowing these wavelengths, extension of the surface actually damps them out. A correlation exists, however, between the width of the $q(\lambda)$ curve derived from infinitesimal-strain modeling (Fig. 7) and the range of wavelengths that show positive growth in the multiple-initial-wavelength simulations. As noted in Section 3.2, the width of the growth curve depends on the thermal gradient of the lithosphere: high temperature gradients produce narrow, sharply peaked $q(\lambda)$ curves and low temperature gradients produce broadly peaked $q(\lambda)$ curves. We expect, therefore, that higher temperature gradients will more easily amplify a single wavelength of the deformation than lower temperature gradients. A comparison of the power spectra of the

15 K km^{-1} and the 30 K km^{-1} simulations shown in Figs. 12D and 12F illustrates this effect. In the 15 K km^{-1} model the power spectrum shows strong amplification of a range of wavelengths between 4.4 and 6.6 km. In contrast, the power spectrum of the 30 K km^{-1} model indicates that growth occurs only in the wavelength range between 3.1 and 3.5 km. Thus while the lower temperature gradient model produces greater-amplitude deformation, the higher temperature gradient model produces deformation with stronger periodicity. We might therefore expect that, on Ganymede, grooved terrain swaths with closely spaced grooves (short wavelengths) would contain a smaller range of wavelengths in their spectra (i.e., be more sinusoidal) than grooved terrain swaths with wide spacings (long wavelengths).

Current observational evidence is inconclusive on this point. Patel et al. (1999) performed a Fourier analysis to determine the dominant wavelengths present in three diverse swaths of grooves within bright terrain and one set of groove lanes within the dark terrain of Nicholson Regio. From this analysis no pattern emerges suggesting that groove swaths with shorter wavelengths (e.g., Uruk Sulcus with a longest dominant wavelength of 3.75 km) are more strongly periodic than groove swaths with longer wavelengths (e.g., Byblus Sulcus with a longest dominant wavelength of 10 km). However, the small number of groove swaths imaged at high enough resolution to accurately measure short topographic wavelengths, and the presentation of the Patel et al. (1999) wavelength data in binned histograms makes a conclusive analysis of variations in periodicity difficult.

Comparison of our numerical results to an analytical prediction of instability growth provides insight into the role of wavelength interactions in creating the surface deformation shown in Fig. 12. Equation (1) gives the final amplitude ($\mathcal{A}_{max}$) produced by instability growth at the dominant wavelength as $\mathcal{A}_{max} = \mathcal{A}_0 \exp[(q_{max} - 1)\dot{\varepsilon}t]$. Likewise, the amplitude of the deformation produced by the growth of a wavelength on the flank of the $q(\lambda)$ curve (Fig. 7) is given by $\mathcal{A}_{flank} = \mathcal{A}_0 \exp[(q_{flank} - 1)\dot{\varepsilon}t]$, where q_{flank} is the growth rate at that particular wavelength. The ratio of the amplitude of the deformation produced at the dominant wavelength to the amplitude of the deformation at a flanking wavelength is then

$$\mathcal{A}_{max}/\mathcal{A}_{flank} = \exp[\Delta q \dot{\varepsilon}t], \qquad (8)$$

where Δq is the difference between the growth rates at the dominant (q_{max}) and flanking (q_{flank}) wavelength. This ratio provides an estimate of how well extension can amplify a single wavelength of deformation when the initial perturbation contains many wavelengths.

We can use the results of Fig. 7 to estimate the $\mathcal{A}_{max}/\mathcal{A}_{flank}$ predicted by our infinitesimal-strain models. For a temperature gradient of 15 K km^{-1} and strain rate of 10^{-13} s^{-1} the growth rate at the dominant wavelength is 8.9. At a wavelength of 3.63 km, on the flank of the $q(\lambda)$ curve, the growth rate is 6. Δq therefore equals 2.9 and, assuming 31.5% extension, $\mathcal{A}_{max}/\mathcal{A}_{flank}$ is 2.5. Thus, one might expect that the amplitude of the dominant wavelength in the multi-wavelength-perturbation model shown in Figs. 12C and 12D should be

about twice the amplitude of the "off-peak" wavelengths. However, examination of the power spectrum shown in Fig. 12D indicates that the dominant wavelength (5 km) has an amplitude ∼4–7 times greater (rather than ∼2.5 times greater) than the flanking wavelength (3.63 km). This suggests that, at finite strains, a nonlinear interaction occurs between growing wavelengths in which faster growth of one particular wavelength inhibits the growth of all other wavelengths, producing more pronounced periodicity than is predicted by Eq. (8), where wavelengths do not interact.

To better understand how wavelengths interact as amplification occurs, we examine how the final form of the topography produced by extending a multi-wavelength perturbation depends on the amplitude of that initial perturbation. Decreasing the amplitude of the initial perturbation to 1.5 m (maximum peak to trough) in cases with $dT/dz = 15$ $\mathrm{K\,km^{-1}}$ and $\dot{\varepsilon} = 10^{-13}$ $\mathrm{s^{-1}}$ produced final topography very similar to Fig. 12C but with ten times smaller amplitude. The amplitude difference between the dominant and "off-peak" wavelengths is reduced relative to that of the 15 m-amplitude perturbation case, however, with the amplitude of the dominant wavelength ∼3.5–4.5 times greater than the amplitude of the off-peak wavelengths. This result suggests that nonlinear effects play a more significant role in instability growth at higher amplitudes. Increasing the amplitude of the initial perturbation to 150 m (maximum peak to trough) more significantly affects instability growth (Figs. 12G and 12H). While the resulting deformation is still periodic with a wavelength near 5 km, a significant short wavelength component of the initial perturbation remains in the topography. The existence of residual topography is permitted by the smaller degree of amplification of the initial perturbation in the 150 m amplitude simulation; extension amplifies the perturbation by a factor of approximately 4–6 in the low amplitude models but by less then a factor of 2 in the 150 m amplitude model. Such small amplification apparently cannot sufficiently remove the short wavelength topography.

The growth of a single dominant wavelength from large-amplitude, random initial topography (as shown in Figs. 12C and 12E) is not an obvious result. One could imagine that, instead of producing periodic deformation, nonlinearities simply amplify whatever irregularities exist in the initial topography, leading to large-scale but irregular (nonperiodic) deformation. In fact, numerical models of finite-amplitude compressional folding support this alternative conception of growth, finding that amplification of an initially random perturbation does *not* immediately lead to deformation that reflects the expected dominant wavelength (Mancktelow, 1999). Instead, these models show that, if initial perturbation amplitudes are large, the initial perturbation geometry exerts a strong influence on the final fold geometry, resulting in large-amplitude deformation that is only quasi-periodic (Mancktelow, 1999). Our results contrast with the results of (Mancktelow, 1999). Even in our large-amplitude initial perturbation simulations, long wavelength initial topography is modified to reflect a single dominant wavelength. We speculate that these differences result from the rather substantial differences in the two model's rheologies and experimental setups.

The results described above provide significant support for the tectonic resurfacing hypothesis. Our modeling indicates that unstable extension can modify small scale (∼10 m or less), random, preexisting topography and replace it, through the action of necking, with moderate amplitude periodic ridges and troughs. Large amplitude topography (∼100 m) is harder to modify due to decreased growth rates at large deformation amplitudes. However, even with random preexisting topography of 100 m, extension produces strongly periodic deformation with an amplitude of several hundred meters.

A number of important questions remain unaddressed by our model. The ability of extensional tectonic deformation alone to completely remove all evidence of the preexisting surface remains unclear. Our results suggest that remnants of large-amplitude, short-wavelength topography, such as crater rims, can remain after groove formation occurs (Fig. 12G), yet observations have not revealed any such "ghost" craters within the grooved terrain on Ganymede. Removal of such short-wavelength topography most likely requires significant faulting to break up and obscure the original terrain. Such faulting is not included in this model. These results also provide little insight into the cause of the grooved terrain's high albedo. Suggestions that tectonic deformation alone can brighten groove terrain by exposing clean ice at the surface cannot be directly tested via this approach, but the relatively low strains present in groove crests (Fig. 6) suggests that, at least in those regions, surface brightening must occur by some mechanism other than tectonic deformation.

4. Sensitivity analysis

The simulations described above treat only the temperature gradient, strain rate, and initial surface topography as free input parameters. However, factors such as the elastic properties of the lithosphere, the grain size of ice, the minimum yield strength of the lithosphere, and the surface temperature can also affect instability growth. We determined the sensitivity of our results to variations in these parameters by fixing the model's temperature gradient at 15 $\mathrm{K\,km^{-1}}$, strain rate at 10^{-13} $\mathrm{s^{-1}}$, and total strain at 31.5% and varying the parameters in question. This analysis provides a more complete understanding of how our results depend on model assumptions.

The elastic parameters of an icy lithosphere are poorly understood. Studies suggest that terrestrial lake and sea ice have average Young's Moduli of 9.3×10^9 Pa (Gammon et al., 1983). This value is insensitive (±1%) to sample age, impurity content, and crystal quality (Gammon et al., 1983). We used a nominal Young's modulus of 10^{10} Pa, in agreement with this value. A fractured lithosphere can experience larger strains at modest stress than an unfractured lithosphere, and this is sometimes modeled with an effective Young's modulus several orders of magnitude smaller than the actual value (Williams and Greeley, 1998). Fig. 13A shows the effect of variations in Young's modulus on the total amount of amplification produced by the necking instability. The amplification is relatively insensitive to the exact value of the Young's modulus over the nominal range of 10^9–10^{10} Pa for intact ice, varying only by a factor
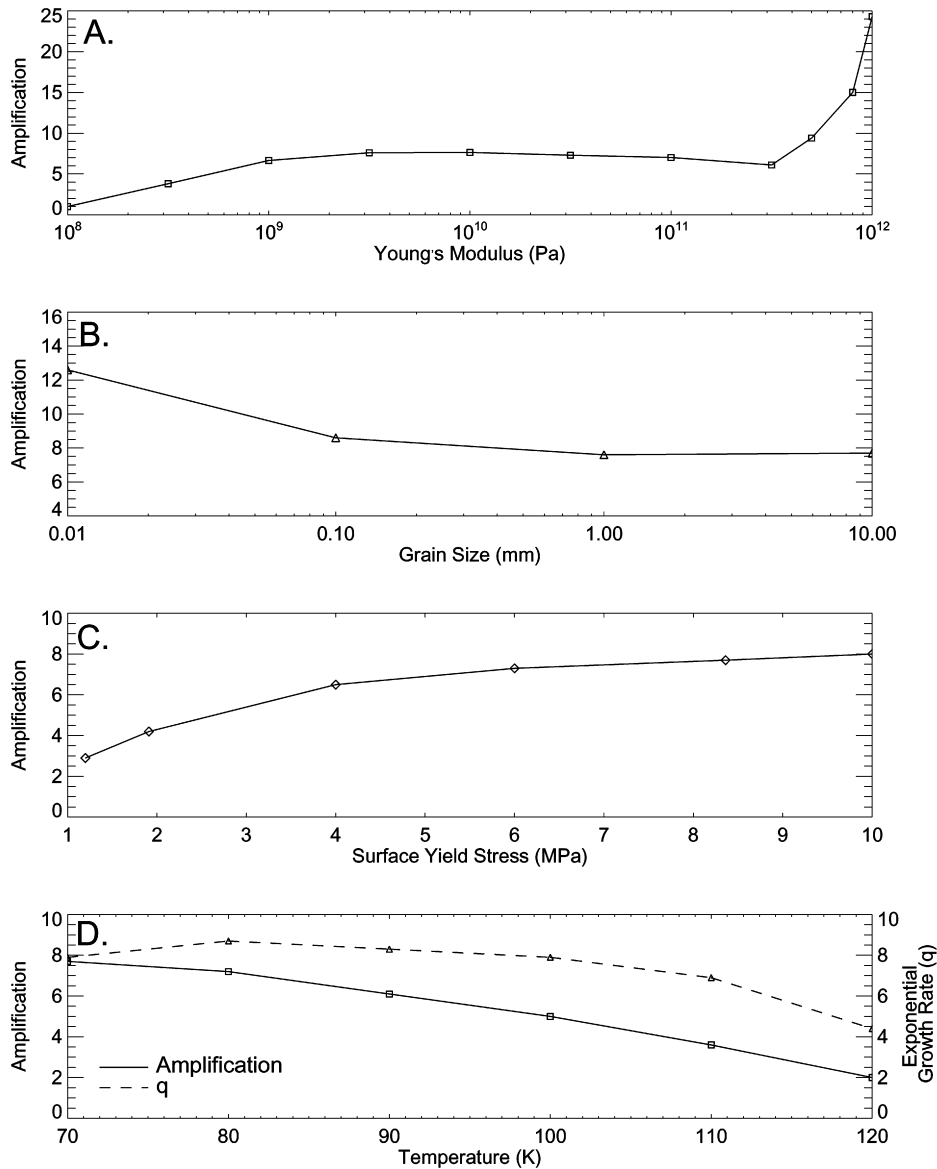
Fig. 13. Amplification as a function of (A) Young's modulus, (B) grain size, and (C) surface yield stress. Amplification (solid lines) and exponential growth rates calculated after 3.15% extension (dashed lines) are also shown in (D). See text for description of results.

of 0.1. At values of Young's modulus less than 10^9 Pa, however, amplification falls off sharply, suggesting that, if Ganymede's lithosphere behaves as a fractured elastic plate, the growth of necking instabilities may be inhibited. However, the applicability of a model with an artificially reduced Young's modulus to a fractured lithosphere remains questionable because the additional strain in a fractured plate is more properly modeled with a brittle (i.e., plastic) rheology than with an artificially compliant elastic system. Very large, if unrealistic, values of Young's modulus (10^{12} Pa) produce significantly more amplification than the nominal cases. This increase occurs because large values of Young's modulus permit the partitioning of more strain into plastic, rather than viscoelastic, deformation. Since necking due to plastic strain is significantly more efficient than necking due to viscous or elastic strain (e.g., Smith, 1975; Fletcher and Hallet, 1983), instability amplification increases.

The grain size of the ice within Ganymede's lithosphere is also poorly constrained. Because grain-size-sensitive GBS flow dominates the viscous rheology of ice under the conditions considered in this model, the choice of grain size can strongly affect the rheological behavior of ice [Eq. (3)]. In zones of high shear, terrestrial sea ice has measured grain sizes of 1–7 mm (Budd and Jacka, 1989). However, the cold surfaces of the Galilean satellites may allow ice grains an order of magnitude smaller to form near the surface. To examine the effect of grain size on our results we compared simulations with grain sizes of 0.01, 0.1, 1, and 10 mm (Fig. 13B). These grain sizes were held spatially and temporally constant throughout the simulation. Variations in grain size over the nominal range (0.1–10 mm) generally do not affect the amount of amplification produced by instability growth. Thus increasing the grain size by an order of magnitude does not appear to sufficiently inhibit the GBS mechanism

to affect the viscous flow at depth. At vary small grain sizes (0.01 mm) amplification is enhanced by a factor of 1.7, suggesting that, if small grain sizes exist in the lithosphere, unstable extension may be enhanced.

Both temperature and stress affect grain size, which can therefore vary spatially and temporally within the lithosphere. Recent modeling of grain size variability in convective systems on icy satellites has illustrated that heterogeneous distributions of grain size not only occur, but directly affect the convective flow (Barr and McKinnon, 2006; Tobie et al., 2006). High near-surface stresses in our simulations favor production of small grain sizes that can enhance strain rates and lead to strain weakening within these zones. This method of strain localization has been shown to be effective for olivine under certain terrestrial conditions (Braun et al., 1999). On the other hand, a reduction in instability growth can occur if high temperature gradients create large-grained ice at depth, reducing the strength contrast between the brittle surface layer and ductile substrate. A full examination of the effects of heterogeneous grain size distributions exceeds the scope of this paper, but understanding its role in instability growth warrants further investigation.

The yielding behavior of ice also strongly affects instability growth. Previous modeling suggests that weak lithospheres (lower yield strength) produce smaller growth rates than strong lithospheres (higher yield strength) (Montési and Collins, 2005). The yield strength of our model lithosphere is given by Eq. (5). Its dependence on a dependent variable (σ_m) makes it difficult to define a minimum yield strength a priori. However, we *can* determine the effect that varying the cohesion (which strongly influences the minimum yield strength) has on our results.

Decreasing the cohesion from our nominal value of 10 MPa ($\sigma_{yield} \sim 8$ MPa at the surface) to 4.7 MPa ($\sigma_{yield} \sim 2$ MPa at the surface) decreases the total amount of amplification by 55% (Fig. 13C). Decreasing the cohesion to even lower values results in unphysical (negative) values of yield strength for typical model stresses. If, as measured by Beeman et al. (1988), the yield strength at the surface is 1.2 MPa, the formation of grooves via unstable extension clearly becomes difficult. These results indicate that, aside from the temperature gradient, strain rate, and total strain, the value of the near surface yield strength is the most important factor in influencing instability growth. Thus the formation of grooved terrain via unstable extensional processes suggests that either the lithosphere behaves relatively strongly, or strain weakening and local heterogeneities can enhance the growth of necking instabilities.

The surface temperature (T_s) can also affect instability growth (Fig. 13D). While growth rates are insensitive to the surface temperature for T_s between 70 and 100 K, simulations with very high surface temperatures ($T_s = 120$ K) have infinitesimal growth rates a factor of 2 smaller than low T_s simulations. Also, because increasing the surface temperature effectively decreases the thickness of the deforming layer, growth saturation (described above) occurs earlier in simulations with high surface temperatures than in simulations with low surface temperatures. Thus despite the insensitivity of initial growth rates to surface temperature, the total amount of amplification produced by extension decreases monotonically with increasing surface temperature. We again suggest that if surface temperatures were ∼100 K or higher, the formation of the grooved terrain via extensional necking requires significant strain weakening or strain localization.

Finally, elucidating how gravitational relaxation, which is naturally included in our model, affected the development of large-scale grooves is essential to understanding the formation of the grooved terrain, a process that may have taken millions of years. Dombard and McKinnon (2006) calculated relaxation timescales for impact craters on Ganymede and Callisto. Using a rheology consistent with our models (although with warmer surface temperatures), they found that, for a surface temperature of 120 K and heat flows of 10 mW m^{-2}, a 25 km crater will relax by ∼10% in 10^7 yrs. In light of these results, we expect that gravitational relaxation can affect the development of ∼10 km wavelength grooves under conditions of low strain rates (long formation timescales) and high heat flow. To test this, we imposed 100 m-amplitude, sinusoidal topography at the surface of a domain with a temperature gradient of 30 K km^{-1}. We separately examined wavelengths of 2 and 10 km, roughly corresponding to the minimum and maximum groove wavelengths produced by our models. The domains relaxed under gravity, without being extended, for a period of 10^7 yrs. We then measured the differences in the horizontal and vertical position of the surface nodes to determine the extent of the gravitational relaxation. We find that negligible relaxation of groove-like structures occurs after 10 million years; topography with wavelengths of 2 and 10 km changed in amplitude by only 1 and 6 m, respectively. We note that the application of tensile stress may increase the rate at which relaxation occurs. Despite this caveat, we conclude that gravitational relaxation plays an insignificant role in necking instability growth. These results are consistent with Dombard and McKinnon (2006) who noted that when surface temperatures are low (80 K), viscus relaxation is inhibited.

5. Implications and conclusion

Our simulations confirm that necking instabilities can occur under a broad range of conditions relevant to Ganymede. At infinitesimal strains, we find that maximum instability growth rates occur at high temperature gradients (⩾45 K km^{-1}) and moderate strain rates (10^{-13} s^{-1}). Dominant wavelengths range from 1.8–16.4 km (post extension), similar to the wavelengths of Ganymede's grooves. These results are qualitatively consistent with previous, linearized, infinitesimal-strain models (Dombard and McKinnon, 2001). We also find, however, that nonlinearities play a crucial role in instability growth at strains exceeding ∼10–20%. Instability growth rates decrease as strains become large, limiting the total amount of amplification that can result from unstable extension. Decline in growth primarily results from the finite thickness of the deforming lithosphere and the extension of the amplifying wavelength, and hence occurs at lower groove amplitudes for high-temperature-gradient, thin-lithosphere models, than for low-temperature-gradient, thick-lithosphere models. This result implies that lin-

ear extrapolation of initial growth rates overpredicts groove heights for large strains. Understanding groove formation at large strains therefore requires the use of finite-strain models.

The inclusion of large strains in the modeling of extensional necking instabilities places new constraints on the formation of Ganymede's grooved terrain. Because instability growth does not continue exponentially at finite strains, the high thermal gradients ($\sim$35 K km^{-1}) required by linear infinitesimal-strain models to produce large amplitude grooves are unnecessary. Instead, thermal gradients as low as 10–20 K km^{-1} are preferred as long as large strains are locally available. This suggests that the formation of grooved terrain required only modest heat fluxes of $\sim$20 mW m^{-2}, rather than the 75 mW m^{-2} predicted by linear models. Such a heat flux would almost certainly have been available on Ganymede as the value falls well below estimates of heat flux derived from the analysis of both furrow systems within Ganymede's dark terrain, and elastic thicknesses near rift zones (McKinnon and Parmentier, 1986; Nimmo et al., 2002).

In addition, we have shown that the formation of necking instabilities can modify preexisting terrains of up to 100-m topography, replacing them with moderate-amplitude, periodically spaced ridges and troughs. These structures are consistent with Ganymede's grooved terrain, although somewhat lower in amplitude. These models provide an important step in quantitatively examining the role of tectonic resurfacing in groove formation.

Our modeling also raises new difficulties for the necking instability model. The use of a more realistic viscoelastic–plastic rheology decreases the initial exponential growth rates by an order of magnitude compared to the results of linear models. These decreased growth rates combine with growth fall-off at large strains to limit the total amplitude of deformation produced by unstable extension. No more than 8-fold amplification of the initial perturbation occurred in any simulation after application of 31.5% strain. Thus, if Ganymede's pre-grooved terrain consisted of $\sim$10 m amplitude topography, extension would produce grooves with amplitudes of $\sim$80 m, a factor of five smaller than is observed. If strains were typically less than 31.5%, the formation of Ganymede's grooved terrain via unstable extension becomes even more difficult. Furthermore, the inclusion of realistic near surface strength profiles, and warmer surface temperatures may further curtail instability growth. We therefore emphasize that forming grooved terrain via unstable extension remains a difficult problem.

The challenges to groove formation may yet be overcome, however, by the inclusion of strain localization mechanisms not considered in the present model. The incorporation of strain or strain-rate softening (i.e., a reduction in the cohesion or effective viscosity of material at high strains or strain-rates, respectively) into numerical models of terrestrial extension strongly affect the model results (Behn et al., 2002; Frederiksen and Braun, 2001; Poliakov and Buck, 1998; Lavier et al., 2000). Frederiksen and Braun (2001) demonstrated that strain softening in the Earth's mantle leads to significant strain localization for a range of assumptions about how softening occurs. Behn et al. (2002) further showed that including strain-rate softening

in models of continental and oceanic rifting led to increases in local strain rates by two orders of magnitude, which in turn led to significantly more surface deformation than in models without strain softening. The inclusion of these processes in our model should have an analogous affect, significantly increasing groove amplification. Furthermore, the presence of discrete faults may also help localize strain. Montési and Collins (2005) found that long-distance fault interactions in an icy lithosphere could lead to structures similar to Ganymede's grooved terrain. Such fault interactions may help to focus strain within extensional necks, and lock-in the amplifying wavelength, preventing the fall-off in growth caused by the shifting wavelength of the perturbation at large strains. The inclusion of these processes appears to be essential to properly modeling groove formation.

The conditions that led to groove formation on Ganymede are not unique in the Solar System. Evidence of extensional tectonics abounds on the icy satellites of both Saturn and Uranus. Our modeling of instability growth at finite strains suggests that the production of significant topography, via unstable extension, does not require high thermal gradients. Furthermore, the low surface temperatures and reduced surface gravity of these small bodies permits higher instability growth rates than on Ganymede (Herrick and Stevenson, 1990). Unstable extension may have therefore played a significant role in modifying not only the surface of Ganymede but also the surfaces of icy satellites such as Enceladus and Miranda.

Acknowledgments

References

Allison, M.L., Clifford, S.M., 1987. Ice-covered water volcanism on Ganymede. J. Geophys. Res. 92, 7865–7876.

Barr, A.C., McKinnon, W.B., 2006. Convection in icy satellites with self-consistent grain size. Lunar Planet. Sci. 37. Abstract 2130.

Barr, A.C., Pappalardo, R.T., 2005. Onset of convection in the icy Galilean satellites: Influence of rheology. J. Geophys. Res. 110, doi:10.1029/2004JE002371. E12005.

Beeman, M., Durham, W.B., Kirby, S.H., 1988. Friction of ice. J. Geophys. Res. 93, 7625–7633.

Behn, M.D., Lin, J., Zuber, M.T., 2002. A continuum mechanics model for normal faulting using a strain-rate softening rheology: Implications for thermal and rheological controls on continental and oceanic rifting. Earth Planet. Sci. Lett. 202, 725–740.

Braun, J., Chéry, J., Poliakov, A., Mainprice, D., Vauchez, A., Tomassi, A., Daignières, M., 1999. A simple parameterization of strain localization in the ductile regime due to grain size reduction: A case study for olivine. J. Geophys. Res. 104, 25167–25181.

Budd, W.F., Jacka, T.H., 1989. A review of ice rheology for ice sheet modeling. Cold Reg. Sci. Technol. 16, 107–144.

Collins, G.C., 2006. Global expansion of Ganymede derived from strain measurements in grooved terrain. Lunar Planet. Sci. 37. Abstract 2007.

Collins, G.C., Head, J.W., Pappalardo, R.T., 1998a. Formation of Ganymede grooved terrain by sequential extensional episodes: Implications of Galileo observations for regional stratigraphy. Icarus 135, 345–359.

Collins, G.C., Head, J.W., Pappalardo, R.T., 1998b. The role of extensional instability in creating Ganymede grooved terrain: Insights from Galileo high-resolution stereo imaging. Geophys. Res. Lett. 25, 233–236.

Dombard, A.J., McKinnon, W.B., 2001. Formation of grooved terrain on Ganymede: Extensional instability mediated by cold, superplastic creep. Icarus 154, 321–336.

Dombard, A.J., McKinnon, W.B., 2006. Elastoviscoplastic relaxation of impact crater topography with application to Ganymede and Callisto. J. Geophys. Res. 111, doi:10.1029/2005JE002445. E01001.

Durham, W.B., Kirby, S.H., Stern, L.A., 1997. Creep of water ices at planetary conditions: A compilation. J. Geophys. Res. 102, 16293–16302.

Fink, J.H., Fletcher, R.C., 1981. Variations in thickness of Ganymede's lithosphere determined by spacings of lineations. Lunar Planet. Sci. 12. Abstract 277.

Fletcher, R.C., Hallet, B., 1983. Unstable extension of the lithosphere: A mechanical model for basin-and-range structure. J. Geophys. Res. 88, 7457–7466.

Frederiksen, S., Braun, J., 2001. Numerical modeling of strain localisation during extension of the continental lithosphere. Earth Planet. Sci. Lett. 188, 241–251.

Gammon, P.H., Klefte, H., Clouter, M.J., 1983. Elastic constants of ice samples by Brillouin spectroscopy. J. Phys. Chem. 87, 4025–4029.

Giese, B., Oberst, J., Roatsch, T., Neukum, G., Head, J.W., Pappalardo, R.T., 1998. The local topography of Uruk Sulcus and Galileo Regio obtained from stereo images. Icarus 135, 303–316.

Goldsby, D.L., Kohlstedt, D.L., 2001. Superplastic deformation of ice: Experimental observations. J. Geophys. Res. 106, 11017–11030.

Golombek, M.P., 1982. Constraints on the expansion of Ganymede and the thickness of the lithosphere. J. Geophys. Res. 87A, 77–83.

Head, J.W., Pappalardo, R.T., Collins, G., Greeley, R., 1997. Tectonic resurfacing on Ganymede and its role in the formation of grooved terrain. Lunar Planet. Sci. 28. Abstract 535–536.

Herrick, D.L., Stevenson, D.J., 1990. Extensional and compressional instabilities in icy satellite lithospheres. Icarus 85, 191–204.

Kirby, S.H., Durham, W.B., Beeman, M.L., Heard, H.C., Daley, M.A., 1987. Inelastic properties of ice I_h at low temperatures and high pressures. J. Phys. 48, 227–232.

Lavier, L.L., Buck, W.R., Poliakov, A.N.B., 2000. Factors controlling normal fault offset in an ideal brittle layer. J. Geophys. Res. 105, 23431–23442.

Mancktelow, N.S., 1999. Finite-element modelling of single-layer folding in elasto-viscous materials: The effect of initial perturbation geometry. J. Struct. Geol. 21, 161–177.

McKinnon, W.B., Parmentier, E.M., 1986. Ganymede and Callisto. In: Burns, J.A., Matthews, M.S. (Eds.), Satellites. Univ. of Arizona Press, Tucson, pp. 718–763.

Melosh, H.J., Raefsky, A., 1980. The dynamical origin of subduction zone topography. Geophys. J. R. Astron. Soc. 60, 333–354.

Montési, L.G.J., Collins, G.C., 2005. On the mechanical origin of two-wavelength tectonics on Ganymede. Lunar Planet. Sci. 36. Abstract 2093.

Nimmo, F., Pappalardo, R.T., Giese, B., 2002. Effective elastic thickness and heat flux estimates on Ganymede. Geophys. Res. Lett. 29, doi:10.1029/2001GL013976. 62.

Owen, D.R.J., Hinton, E., 1980. Finite Elements in Plasticity: Theory and Practice. Pineridge Press Limited, Swansea, UK.

Pappalardo, R.T., Collins, G.C., 2005. Strained craters on Ganymede. J. Struct. Geol. 27, 827–838.

Pappalardo, R.T., Head, J.W., Collins, G.C., Kirk, R.L., Neukum, G., Oberst, J., Giese, B., Greeley, R., Chapman, C.R., Helfenstein, P., Moore, J.M., McEwen, A., Tufts, B.R., Senske, D.A., Breneman, H.H., Klaasen, K., 1998. Grooved terrain on Ganymede: First results from Galileo high-resolution imaging. Icarus 135, 276–302.

Pappalardo, R.T., Collins, G.C., Head, J.W., Helfenstein, P., McCord, T.B., Moore, J.M., Prockter, L.M., Schenk, P.M., Spencer, J.R., 2004. Geology of Ganymede. In: Bagnell, F., Dowling, T. (Eds.), Jupiter. The Planet, Satellites and Magnetosphere. Cambridge Univ. Press, Cambridge, pp. 363–396.

Parmentier, E.M., Squyres, S.W., Head, J.W., Allison, M.L., 1982. The tectonics of Ganymede. Nature 295, 290–293.

Patel, J.G., Pappalardo, R.T., Head, J.W., Collins, G.C., Hiesinger, H., Sun, J., 1999. Topographic wavelengths of Ganymede groove lanes from Fourier analysis of Galileo images. J. Geophys. Res. 104, 24057–24074.

Patterson, W.S.B., 1969. The Physics of Glaciers. Pergamon Press, New York.

Poliakov, A.N.B., Buck, W.R., 1998. Mechanics of stretching elastic–plastic–viscous layers: Applications to slow-spreading mid-ocean ridges. In: Buck, W.R., Delaney, P.T., Karson, J.A., Lagabrielle, Y. (Eds.), Faulting and Magmatism at Mid-Ocean Ridges. American Geophysical Union, Washington, DC, pp. 305–323.

Ranalli, G., 1995. Rheology of the Earth. Chapman and Hall, London.

Schenk, P.M., McKinnon, W.B., Gwynn, D., Moore, J.M., 2001. Flooding of Ganymede's bright terrains by low-viscosity water–ice lavas. Nature 410, 57–60.

Showman, A.P., Malhotra, R., 1997. Tidal evolution into the Laplace resonance and the resurfacing of Ganymede. Icarus 127, 93–111.

Showman, A.P., Stevenson, D.J., Malhotra, R., 1997. Coupled orbital and thermal evolution of Ganymede. Icarus 129, 367–383.

Showman, A.P., Mosqueira, I., Head, J.W., 2004. On the resurfacing of Ganymede by liquid–water volcanism. Icarus 172, 625–640.

Smith, R.B., 1975. Unified theory of the onset of folding, boudinage, and mullion structure. Geol. Soc. Am. Bull. 86, 1601–1609.

Smith, B.A., Soderblom, L.A., Beebe, R., Boyce, J., Briggs, G., Carr, M., Collins, S.A., Cook, A.F., Danielson, G.E., Davies, M.E., Hunt, G.E., Ingersoll, A., Johnson, T.V., Masursky, H., McCauley, J., Morrison, D., Owen, T., Sagen, C., Shoemaker, E.M., Strom, R., Suomi, V.E., Veverka, J., 1979a. The Galilean satellites and Jupiter: Voyager 2 imaging science results. Science 206, 927–950.

Smith, B.A., Soderblom, L.A., Johnson, T.V., Ingersoll, A.P., Collins, S.A., Shoemaker, E.M., Hunt, G.E., Masursky, H., Carr, M.H., Davies, M.E., Cook, A.F., Boyce, J.M., Danielson, G.E., Owen, T., Sagan, C., Beebe, R.F., Veverka, J., Strom, R.G., McCauley, J.F., Morrison, D., Briggs, G.A., Suomi, V.E., 1979b. The Jupiter system through the eyes of Voyager 1. Science 204, 951–972.

Squyres, S.W., 1980. Volume changes in Ganymede and Callisto and the origin of grooved terrain. Geophys. Res. Lett. 7, 593–596.

Squyres, S.W., 1981. The topography of Ganymede's grooved terrain. Icarus 46, 156–168.

Squyres, S.W., 1982. The evolution of tectonic features on Ganymede. Icarus 52, 545–559.

Tobie, G., Duval, P., Sotin, C., 2006. Grain size controlling processes within Europa's ice shell. Lunar Planet. Sci. 37. Abstract 2125.

Turcotte, D.L., Schubert, G., 2002. Geodynamics. Cambridge Univ. Press, Cambridge.

Williams, K.K., Greeley, R., 1998. Estimates of ice thickness in the Conamara Chaos region of Europa. Geophys. Res. Lett. 25, 4273–4276.

Zahnle, K., Schenk, P., Levison, H.F., Dones, L., 2003. Cratering rates in the outer Solar System. Icarus 163, 263–289.

Zuber, M.T., Parmentier, E.M., 1996. Finite amplitude folding of a continuously viscosity-stratified lithosphere. J. Geophys. Res. 101, 5489–5498.